Spring 2010

# Full-scale two-phase flow measurements using optical probes on Athena II research vessel

James Paul Johansen
*University of Iowa*

# FULL-SCALE TWO-PHASE FLOW MEASUREMENTS USING OPTICAL PROBES ON ATHENA II RESEARCH VESSEL

by

James Paul Johansen

A thesis submitted in partial fulfillment
of the requirements for the Master of
Science degree in Mechanical Engineering
in the Graduate College of
The University of Iowa

May 2010

Thesis Supervisor: Associate Professor Pablo M. Carrica

Graduate College
The University of Iowa
Iowa City, Iowa

CERTIFICATE OF APPROVAL

_____

MASTER'S THESIS

_____

This is to certify that the Master's thesis of

James Paul Johansen

has been approved by the Examining Committee
for the thesis requirement for the Master of Science
degree in Mechanical Engineering at the May 2010 graduation.

Thesis Committee: _____
Pablo M. Carrica, Thesis Supervisor

_____
Frederick Stern

_____
Albert Ratner

To my family

The well being of the world largely depends upon the work of the engineer. There is a great future and unlimited scope for the profession; new works of all kinds are and will be required in every country, and for a young man of imagination and keenness I cannot conceive a more attractive profession. Imagination is necessary as well as scientific knowledge.

Sir William Halcrow
Addressing the Institution of Civil Engineers

ACKNOWLEDGMENTS

I would like to first acknowledge the IIHR-Hydroscience and Engineering program for allowing me to pursue my graduate studies and research at The University of Iowa. This work was supported by the US Office of Naval Research grant N00014-08-1-1083, under administration of Dr. Patrick Purtell. The help of Dr. Mark Hyman during planning and experimentation is deeply appreciated.

I would like to thank my advisor, associate professor Pablo Carrica. His encouragement and expertise helped me along my journey through graduate school to publish a paper and write this thesis. His guidance and willingness to help develop me as a researcher has influenced my approach to science more than anyone and I am grateful to him for his time, critique and friendship. Another thank-you is due to my other committee members, Frederick Stern and Albert Ratner, who have taken time out of their busy schedule to review my written thesis and listen to my oral defense.

I would like to thank the members of the IIHR shop Pete Haug, Jim Goss, Doug Houser and especially Mike Anderson for helping give direction in the shop, assemble the electronics, weld the positioning system and machine parts for our experimental set up. I would like to thank the administrative staff including Melissa Eckrich, Teresa Gaffey, Laura Myers, Margaret Evans and especially Jennifer Rumping who could answer any administrative question imaginable. I would like to thank Alejandro Castro whom was instrumental in the solving the bubble unfolding problem.

Finally I would like thank my fiancée Melissa Johnson for using her English skills to edit my thesis and all of my friends and family for their support and companionship during my studies.

ABSTRACT

Measurements of gas volume fraction, bubble velocity, chord length and bubble size distributions were performed in the research vessel *Athena II* operating in Saint Andrew Bay in the gulf coast near Panama City, FL. Double tipped sapphire optical local phase-detection probes were used to acquire indicator functions downstream of the breaking bow wave, behind the masker and at the stern. These indicator functions were also taken at different depths, distances from the hull, operating speeds and headings respect to the waves. The data processing includes the computation of velocity of individual bubbles and chord lengths, resulting in chord length distributions. These chord length distributions are used to obtain bubble size distributions using a novel procedure described in detail. Uncertainty analysis is performed for gas volume fraction, average bubble velocity and chord length. The results indicate that air entrainment increases with ship speed and sailing against the waves at all positions. The bow wave exhibits unsteady breaking that creates bubble clouds, which were characterized and identified by signal processing. At the stern a very strong dependence of bubble size with depth was found, with evidence that bubbles smaller than 500 $\mu m$ are transported through the bottom of the hull and reach the transom. The roller present at the transom, the associated strong unsteadiness and bubble entrainment are well captured, as indicated by the stern results, showing the frothy nature of the upper layer.

TABLE OF CONTENTS

LIST OF TABLES

LIST OF FIGURES

# CHAPTER 1

# INTRODUCTION

This thesis presents introduction, design setup, data acquisition and the analysis of multiphase flow full-scale experiments on the navy research vessel ship the *Athena II*. The data was gathered using double tipped sapphire optical local phase-detection probes. The results from this study are:

1. Gas volume fraction profiles.
2. Computation of individual bubble velocity and chord lengths.
3. Chord length profiles that are *unfolded* in a technique to yield bubble size distributions.
4. Bubble cloud identification and characterization.
5. Uncertainty analysis for gas volume fraction, average bubble velocity and chord length.

The data reduction processes presented herein is novel and is explained in detail.

## 1.1. Problem Statement

Multiphase flows are complex phenomena that are difficult to measure in full-scale experiments, making them extremely challenging problems in ship research. Air and water multiphase flows typically originate in areas of high turbulence at the interface between air and water. Man-made spillways and ship wakes often create turbulence high enough to entrain bubbles of various sizes meters into water. The air phase in a multiphase flow tends to gravitate toward regions of lower pressure due to its low density. In regions of extreme low pressure cavitation can occur which seeds bubbles by creating water vapor pockets. The water in these pockets is only turned into vapor by the extreme low pressures but dissolved gasses present in the water are also drawn out in the water vapor pocket. Once the pressure resumes to normal a majority of the water vapor

condenses leaving micro bubbles of previously dissolved gas. These gas bubbles take usually take a longer time to dissolve than it takes to enter the bubbly wake and float slowly to the free surface.

Two-phase flows around ships have been studied for years, mostly in relation to the acoustic signatures of ships; ships have been tracked acoustically since before World War II (Borowski et al. 2008). Bubbles can be generated by the ship's bow and corresponding shoulder breaking waves, the hull/free surface contact line, the propeller and the highly turbulent stern flow. In these regions two-phase flows are formed and transported by the flow below the hull and in the bubbly wake, which can be kilometers long. More recently, bubble-induced drag reduction has attracted increasing interest. Externally-injected bubbles have achieved drag reductions ranging from 4% to 22% in ships and flat plates (Latorre et al. 2003, Takahashi et al. 2003). During normal operation self-aeration of a ship likely has an effect on drag, although it is very difficult to quantify since two-phase phenomena do not exhibit similarity at model scale, forcing experimentation in full-scale. Though significant effort has been devoted to the study of ship's wakes and far-field measurements (see for instance Hyman 1994, Caruthers et al. 2009), little is known about the sources of bubbles; whether a majority of the deep bubbles are created where the free surface meets the ship hull or created by cavitation in the low pressure regions near the ship propeller is still unknown. Near-field models have long relied on assumed bubble size distributions, like that mentioned in Cartmill and Su (1993), and imposed entrainment locations to predict the two-phase field (Carrica et al. 1998, Carrica et al. 1999). Some progress has been recently made in predicting the location and intensities of the bubble entrainment (Moraga et al. 2008, Ma et al. 2009), but calibration of the models is based on simple model-scale canonical problems and validation based on ship computations, and full-scale measurements have not been performed.

Near-field full-scale measurements of the two-phase flow around a ship are scarce, mostly due to the difficulties related with operating at bubble-generating speeds and instrumentation limitations. Wakes are generally measured in the earth system, where velocities are fairly small, while near-field measurements need to be made on board in velocities proportional to ship speed. Acoustic methods can be used in the far field to obtain air concentration and bubble size distributions, while in the near field the presence of the hull makes it difficult to use these methods. In one of the few near-field full-scale measurements known to the authors, Terrill and coworkers (Terrill and Fu 2008) used an array of 12 conductivity probes to measure the gas volume fraction on the highly aerated stern regions of the *Revelle* and the US Navy *Athena* research vessel II (*Athena II* R/V). Measurements for *Athena II* R/V were performed during the May 2004 campaign at different depths and lateral positions for speeds ranging from 1 to 6.6 m/s (2 to 12.8 knots). These measurements revealed the presence of a sharp decrease on the gas volume fraction with depth, separating the recirculating region behind the stern above the transom bottom corner with the boundary layer developed by the hull. Optical sizing measurements performed below the hull line at the transom, in regions of low gas volume fraction, resulted in a peak in the bubble size distribution (in $bubbles/\left(m^3 \mu m\right)$) for bubbles at around 15 $\mu m$ in radius (Terrill et al. 2005). Jeon (Jeon et al. 2008) used a defocused digital particle image velocimetry (DPIV) system to measure bubble size distribution and gas volume fraction on the previously mentioned *Athena II* R/V in the May 2004 experimental campaign. The system was limited to maximum gas volume fractions of about 1% due to bubble saturation in the measurement domain, therefore two deep regions downstream of the transom were measured due to the lower gas volume fractions rather than close to the stern. Average bubble sizes are reported for two salinity concentrations and several speeds, ranging from 1 to 6.2 m/s (2 to 12 knots).

This work presents full-scale measurements of gas volume fraction, bubble velocity and bubble size distribution for the *Athena II* R/V. The measurements were

performed using double tipped optical local phase-detection sapphire probes, which by sensing phase interfaces provide the phase indicator function in a point in space for a period of time. Using double tipped probes allows measurement of the bubble velocity and the size distribution, after some assumptions. The two-phase parameters were measured downstream of the bow breaking wave, the aerator masker and in the highly ventilated transom stern flow, for velocities ranging from 3.1 to 6.2 m/s (6 to 12 knots).

The use of optical phase-detection probes provides detailed information at a single point, but significant challenges had to be considered and overcome before they were used in a full-scale ship in the ocean. These included issues such as fouling, debris, and mechanical vibrations due to high drag forces. Fouling is the accumulation of unwanted materials on the optical probe tips. Glass fiber optics probes are relatively easy to manufacture with small active tips (see for example Hoschek et al. 2008), but are fragile and therefore unsuitable for full-scale ship experiments. Sapphire probes are significantly more difficult to build, but offer a remarkable resilience compared to glass probes. Former applications in hostile environments include study of aeration ditches (Vermande et al. 2007), steam/water flows (Yoneda et al. 2002) and unsteady cavitation (Stutz and Reboud 1997). Most studies found in the literature use sapphire probes manufactured by RBI in Meylan, France. In this work two types of sapphire probes from RBI are used, made from polished 375 $\mu m$ and 390 $\mu m$ sapphire rods. In addition, the authors manufactured a smaller probe made of 125 $\mu m$ sapphire fibers which provided less flow intrusiveness and resulted in better cross-correlation.

# CHAPTER 2

# FULL-SCALE EXPERIMENT IN ATHENA II R/V

## 2.1. Experimental Conditions

Experiments were performed aboard the US Navy research vessel *Athena II*, a decommissioned PG-84 Asheville-class patrol gunboat transformed into a high-speed research vessel in 1976 and shown in Fig. 1. As the PG-84 the ship served a tour of over eight years providing coastal surveillance and gunfire support for the American and South Vietnam forces in the Vietnam War (McManuels 2006). The water line length of the *Athena II* is $L = 47\,m$, with a beam of $B = 7.32\,m$ which is the ship width at its widest point and a design draft, or distance from waterline to keel, of $T = 3.2\,m$. The *Athena II* has an aluminum hull, resulting in a water displacement of 240 tons. The *Athena II* R/V is fitted with a skeg, which is a long fin-like protrusion mounted along the keel beginning at mid-ship and ending near where the propeller shafts exit the hull, as seen in the bottom graphic of Fig. 1. The *Athena II* is also fitted with starboard and port roll stabilizers shown in the bottom graphic of Fig. 1. The ship has a compound masker system to entrain bubbles and reduce the ship's radiated noise. The masker is a protruding ring fitted around the hull at approximately $x/L = 0.45$. The bubbly white water produced by the masker can be seen in Fig. 1. Propulsion of the *Athena II* is provided by twin counter-rotating propellers of variable pitch, powered either by two independent diesel engines or a GE LM 1500 gas turbine, allowing the vessel to reach maximum speeds of 6.7 or 18 m/s using diesel or gas turbine, respectively.

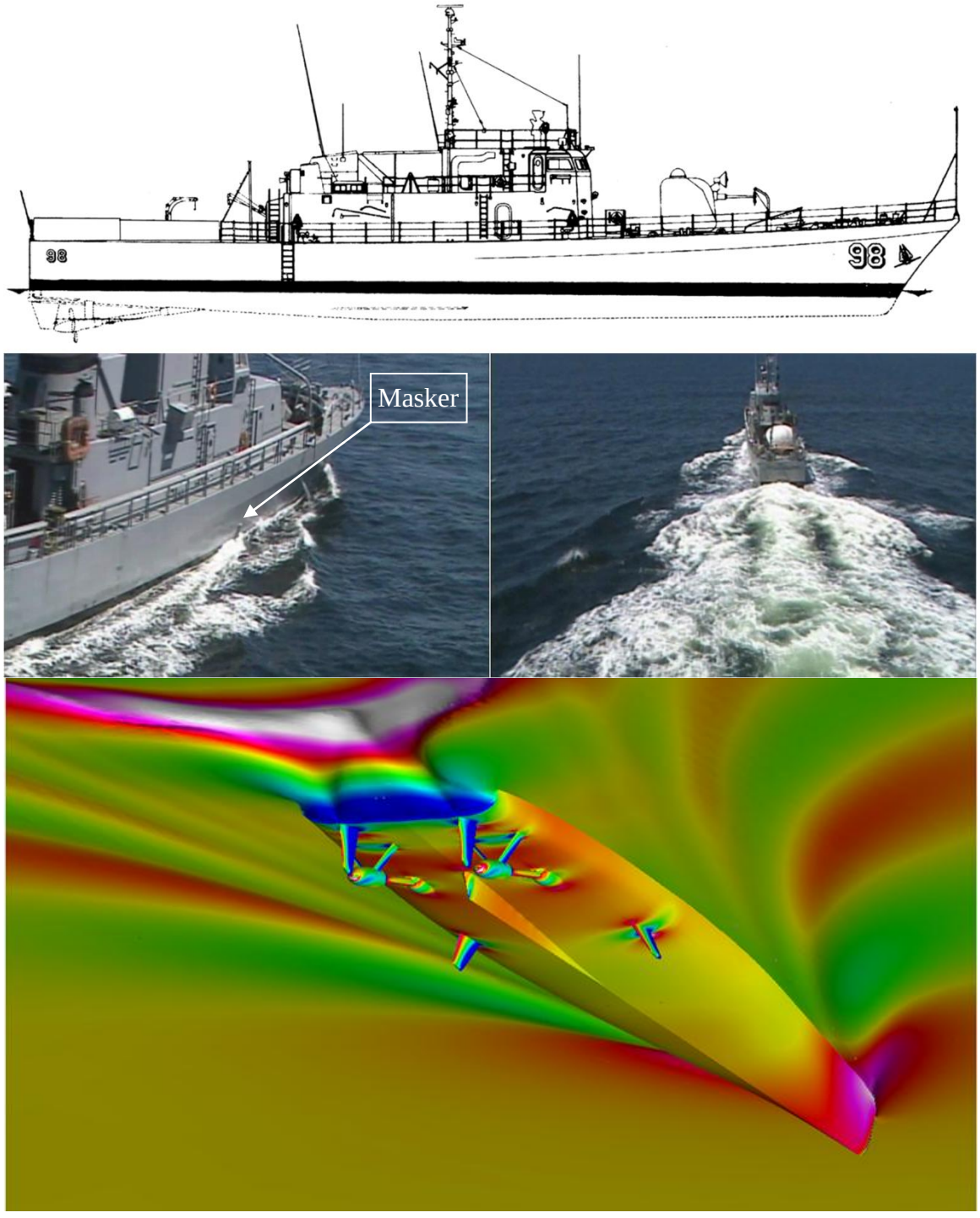


Figure 1: *Athena II* R/V. Top: schematic of the ship, waterline and appendages. Middle left: view of the bow wave and the masker. Middle right: bubbly wake produced by the ship. Bottom: underside of the ship clearly showing the skeg and starboard and port roll stabilizers by Xing et al (2009).

The measurement campaign took place in Panama City, FL, where the *Athena II* R/V is based out of the US Naval Surface Warfare Center, in the week of April 20 to 24, 2009. Measurements were taken Tuesday through Friday in Saint Andrews Bay and in the Gulf of Mexico several miles offshore but within sight of the coast. Measurements were taken at the positions shown in Fig. 2, located downstream of the unsteady breaking bow wave, the starboard masker and the port side of the stern.

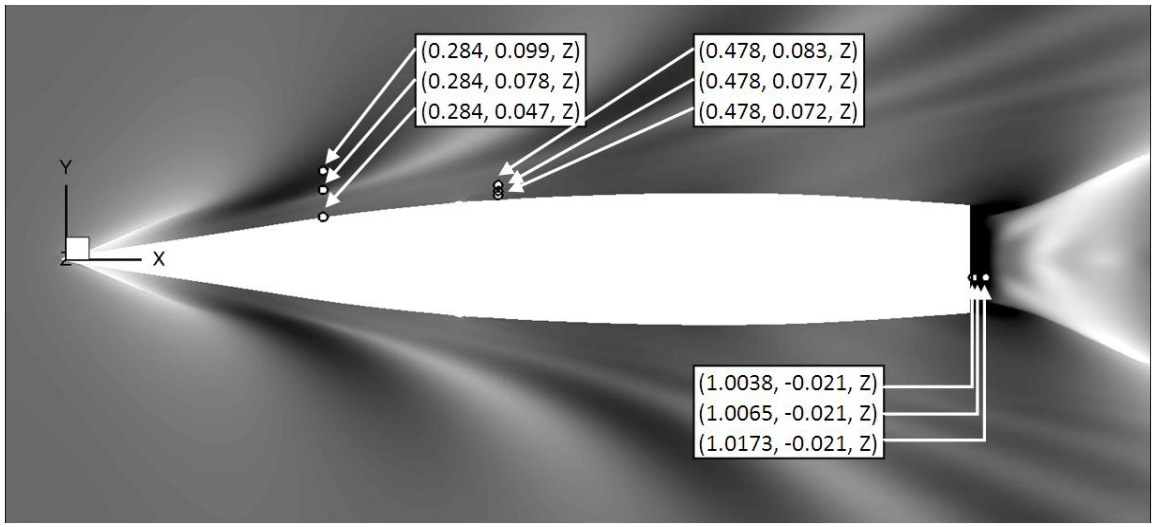


Figure 2: Athena R/V profile at waterline showing probe measurement locations and free surface.

## 2.2. Optical Phase-Detection Probes Overview

### 2.2.1. Probe Principles

Intrusive optical phase detection probes are designed to pierce bubbles and droplets in two-phase air water flows. Phase detection probes distinguish between air and water by detecting the difference in the refraction index between the phases. Optical

phase detection probes are used to measure the phase indicator function, defined as (Ishii 1975)

$$\chi(\mathbf{r},t)=\begin{cases}1 & \textit{if the probe tip is in air}\\ 0 & \textit{if the probe tip is in water}\end{cases} \tag{1}$$

The operating principle is usually described using the Snell-Descartes refraction law, which states

$$n_f \sin i = n_k \sin r \tag{2}$$

To measure the indicator function, light is emitted through a glass optical fiber with a core of index of refraction $n_f$ and some of the emitted light is reflected back according to the refractive index of the surrounding medium $n_k$. In the above equation *i* and *r* are angles in respect to a line normal to the glass-fluid interface plane. Total reflection occurs for a light off a surface for *i* greater than $i_c$ the critical angle found by

$$i_c = \arcsin\left(\frac{n_k}{n_f}\right) \tag{3}$$

Using Eq. (3) one can calculate a range of possible probe tip angles that could differentiate phases, but it has been shown that phase detection can occur for square tips and very sharp angles (Cartiellier and Achard 1991). This is most likely due to the fact that the light rays arrive at the glass-fluid interface in a range of angles. While some additional information on the instrumentation used is provided in Section 2.3., a detailed discussion of working principles of optical phase detection probes and conductivity probes is covered by (Cartellier and Achard 1991, Barrau *et al*. 1999).

Three probes were employed in the experiments. For the masker and transom measurements a double sapphire tip RBI probe was used, made of 375 $\mu m$ sapphire rod polished to a cone of about 15 degrees down to a tip finished with a 45 degree cone with an effective radius of about 30 $\mu m$, shown in Figs. 3a and 3c.

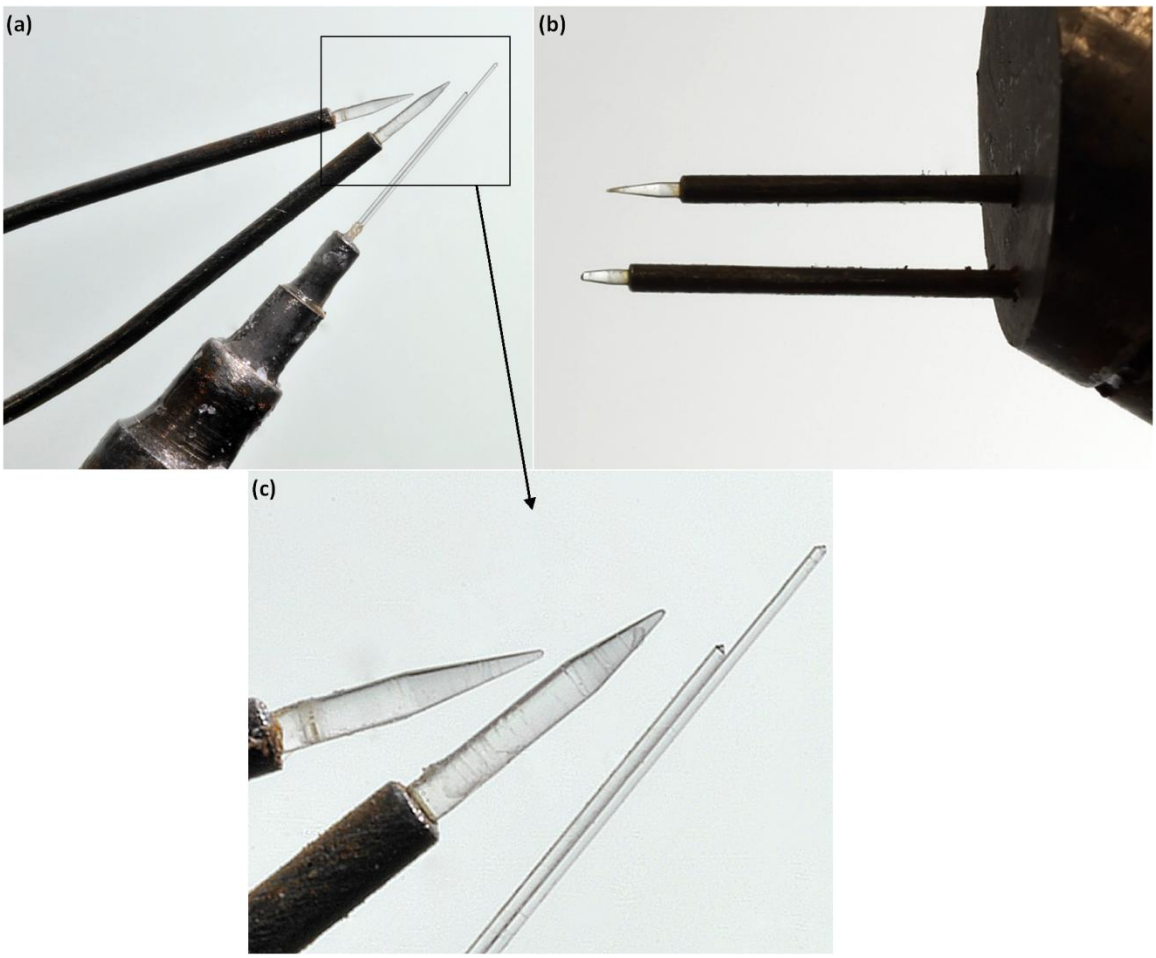


Figure 3: Optical probes. (a) RBI (left) and IIHR (right), (b) RBI II, (c) close-up of the tips of RBI and IIHR probes.

For the bow measurements, a smaller double probe was constructed using 125 $\mu m$ sapphire fiber polished to a 45 degree cone on the tip, as shown in Figs. 3a and 3c, resulting in a less intrusive system with better cross-correlation between the two tips of the probe. The polishing of the 45 degree cone was carried out by a double rotation grinding technique. The tip was put to a bench top lapidary grinding wheel with 1 $\mu m$ grit diamond abrasive paper. The sapphire fiber was held by a rotating Dremel extension bit providing the second level of rotation. This double rotation grinding action allowed for high quality tips to be produced. On the end opposite the polished cone the short sapphire

fiber was polished to 90 degrees and spliced with a glass fiber with 100/140 $\mu m$ core/cladding diameters made by TLC/Corning. This probe will be referred to as the IIHR probe as it was produced in an IIHR laboratory. A second, sturdier probe made by RBI with 390 $\mu m$ sapphire rod was also used for measurements at the bow under rougher seas, see Fig. 3b. This probe is hereafter referred to as RBI II. The distance between tips for the RBI probe was 1.2 *mm*, 2.25 *mm* for the RBI II probe, and 1.32 *mm* for the IIHR probe.

## 2.3. Instrumentation

The instrumentation for one channel or one probe tip is composed by optical and electronic modules, consisting of a light source, a photodetector and an optical fiber connector for the probe itself, with a fiber optic coupler connecting all these components, plus amplifiers, signal conditioners and comparators. The light source directs light through fiber optics to a fiber optic coupler, which works as a reverse beam splitter. This beam splitter sends 50% of the incoming light to an optical fiber connector to which the probe is attached. Due to refraction index variations between air and water and the conical shape of the probe tip, more light is reflected back to the coupler when the probe tip is in air. Once the light reflect from the probe the coupler acts as a true beam splitter and transmits a fraction of the light that is reflected from the probe back to the photodetector which converts light into electric signals that are then conditioned and amplified. The analog signals are subsequently transformed into binary phase indicator functions using a double threshold technique (Cartellier and Achard 1991). In this work RBI infrared optoelectronic modules were used.

In the RBI system the binary signals from each of the channels are fed to a USB card with a 1 $\mu s$ resolution that connects directly to a laptop PC. RBI proprietary software ISO was used to acquire the data, which was stored for off-line analysis. All of the

instrumentation was mounted in sturdy aluminum cases consisting of four optoelectronic channels, two dual channel oscilloscopes for monitoring the analog signals, a UPS backup power module, a USB card and a multimeter to monitor the threshold levels.

From the indicator function, the time-averaged gas volume fraction is computed from:

$$\alpha(\mathbf{r}) = \frac{1}{T}\int_0^T \chi(\mathbf{r},\tau)\,d\tau \qquad (4)$$

where $T$ is the averaging period. $T$ has to be long enough such that the gas volume fraction converges to a steady value. Following Carrica *et al*. (1995), this means that enough bubbles are measured and that the integration time is significantly longer than the characteristic time of whatever transient physical process is occurring in the two-phase flow. To converge other variables, such as the bubble size distribution, significantly longer times are needed. In this work measurement times ranges from 1 to 3 minutes, limited by the ability of the ship to maintain steady conditions. In most conditions several measurements were taken to check repeatability and to reduce statistical errors, as discussed later.

## 2.4. *Athena II* Experimentation Procedure and Implementation

### 2.4.1. Probe Deployment

To make measurements on the ship the electronics cases had to be anchored securely to the hull so that wave motion would not disrupt data collection. The PC had to then be connected to the USB of the data acquisition system. Once the electronics were powered on the desired probes, optical cables had to be connected to the optoelectronic unit. The optical cables for optical probes are very fragile as they cannot have small bend

radii. One of the auxiliary probes brought for experimentation was destroyed by deployment because of optical cable damage. However, this was mainly due to a design flaw in the cable used, where there was a hollow area between the interior fiber and the cable protective coating allowing for easy crimping. For protection of the optical cable from drag from the sea it had to be fastened to the positioning system's vertical pole during measurement.

The probes were deployed at different locations around the hull of the *Athena II* R/V by adjustment of a positioning system designed specifically for these experiments. The positioning system consisted of a vertical pole made of thick-walled steel tube 25.4 mm in diameter, with the last meter of the measuring end reduced to a 12.7 mm diameter pole that was fixed out from the deck above the area of water where the measurements were to be taken. Two horizontal brackets held the vertical pole away from the ship. The brackets were built to attach onto the 50.8 mm stanchions, which are handrail poles, surrounding the ship so measurements in different locations along the hull could be facilitated. The vertical pole off the side of ship fit in tubes, welded to the end of the stanchion brackets, of a larger diameter than the vertical pole so the pole could be easily raised or lowered inside the tubes to measure different depths. At the bottom of the pole the probe was fastened securely, ready to be immersed in the sea for measurement. When the appropriate depth for measurement was set the vertical pole was locked in the tube by set screws threaded into the side of the tube in both the top and bottom stanchion brackets. The top horizontal stanchion bracket could also be constricted or elongated by a horizontal version of the same concentric tube design used for the vertical positioning. By making the top horizontal stanchion bracket longer or shorter than the lower stanchion bracket the measuring pole would no longer be perfectly vertical and a non-ninety degree angle would be created between the horizontal stanchion brackets and the now non-vertical pole. There were hinges on the horizontal stanchion brackets near the vertical

pole side of the bracket to allow the non-ninety degree situation to occur without breaking the brackets. The extensible hinged horizontal stanchion bracket permitted positioning of the probe normal to the hull. To perform measurements at the stern, where no stanchions were available, a 50.8 mm vertical tube was attached to existing brackets welded on the transom face of the hull, and then the same positioning system was used.

### 2.4.2. Threshold Calibration

After the probes were deployed the signal had to be appropriately calibrated to pass the thresholds properly. This has to be done anew for each probe deployment due to changes in design between different probes and lighting conditions. To begin the calibration the threshold voltages in the optoelectronic must be mechanically set by turning a screw in the back of the unit to recommended values approximately one and four volts. A multimeter must be used to read the threshold voltages in the RBI optoelectronic units. The probe must then be put in water to set the water phase to zero volts by turning a knob in the front of the optoelectronic unit. The probe is then put in air to set the air phase voltage to five volts by turning the gain screw in the front of the optoelectronic unit. If the screw is not able to attain the necessary gain there is a knob that can be switched to attain higher levels of gain. Once the thresholds and signal is calibrated the probe measurement can take place. The signal zero value has to be periodically checked through the oscilloscope display and adjustments made during experimentation to make sure the signals are passing the thresholds during phase changes.

# CHAPTER 3

# DATA PROCESSING

The measurements provided two indicator functions, corresponding to each tip of the probe used. These indicator functions were processed to account for stratification, to obtain gas volume fraction, bubble velocity, bubble size distribution, and to identify bubble clouds.

## 3.1. Raw Indicator Function

Fig. 4a shows eight seconds of the indicator functions measured at the bow with the IIHR probe. An excellent correlation between the probes can be observed, helped by the small size of the probe tips and by the high bubble velocity. As shown in Eq. (1), a logical level of 1 corresponds to the air phase. Fig. 4b shows a larger view of a typical single bubble event with the times of phase change displayed. Defining the rising and falling times for the same bubble *i* for Probe Tip 1 as $(t1_{i+}, t1_{i-})$ and for Probe Tip 2 as $(t2_{i+}, t2_{i-})$, the time the probe tip was inside each bubble can be found on an event by event basis for Probe Tip 2 $\Delta t1_i$ and Probe Tip 2 $\Delta t2_i$ as

$$\Delta t1_i = t1_{i-} - t1_{i+} \tag{5}$$

$$\Delta t2_i = t2_{i-} - t2_{i+} \tag{6}$$

Notice in Fig. 4a that there is large time period in air starting at the 18.3 second mark indicating that the probe was out of the water for a period of time. This happened when the probe was very close to the air/water interface, due to the presence of small waves, or when the free surface was highly unsteady, as in the stern region.

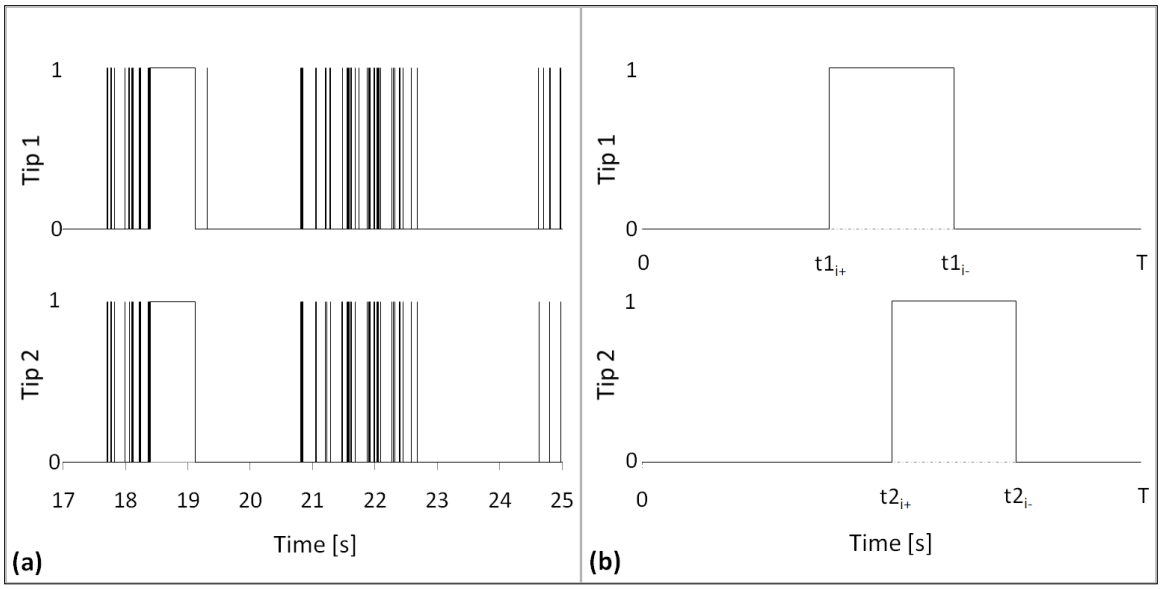


Figure 4: (a) Typical indicator functions from experimental data sample, (b) larger view of an idealized single bubble event in both probe tips.

## 3.2. Indicator Function Filtering

The first step in signal processing is the removal of the time when the probe breaks the free surface. The probe is no longer in the air water mixture resulting in artificially higher recorded gas volume fraction. The logical filter expression is

$$\boxed{\begin{array}{l} if: \Delta t1_i > \dfrac{CL_{max}}{V_{ship}} \\ \quad then: \Delta t1_i = out\ of\ water\ time \end{array}}$$

where $CL_{max}$ is the maximum bubble chord length, set to 10 *mm*, and $V_{ship}$ is the ship velocity. The new filtered gas volume fraction $\alpha 1_{filter}$ expression is

$$\alpha 1_{filter} = \frac{\sum_{i=1}^{N_1 - N_{1o}} (\Delta t1_i)[in\ water] - \sum_{i=1}^{N_{1o}} (\Delta t1_i)[out\ of\ water]}{T - \sum_{i=1}^{N_{1o}} (\Delta t1_i)[out\ of\ water]} \qquad (7)$$

where $T$ is the sampling time, $N_1$ is the number of bubbles detected by Tip 1 and $N_{1o}$ is the number of out-of-water events.

The measured indicator functions for both tips do not correlate exactly, i.e. the signal of the second probe is not a perfect shift in time of the signal of the first probe. Herein we attempt to pair the bubbles detected by Tip 1 to those of Tip 2 by applying a series of filters to the indicator functions. This allows determination of velocity and chord length for each bubble, and the corresponding bubble velocity and size distributions. Four logical filters are used for this purpose.

The first logical filter is to limit possible accepted bubble velocities by assuming that the probe is in the direction of the flow and there is a range of velocity fluctuations around the velocity obtained by cross-correlation of the signal, $V_{cc}$. A range $V_\Delta$ of approximately $\pm 3$ m/s around the cross-correlation velocity was used on the bow and masker sections of the ship. In the stern section the range of bubble velocities increased due to the more complex multidirectional flow structures. The logical expression is

$$\begin{aligned} &if: V_{cc} - V_\Delta < V_i < V_{cc} + V_\Delta \\ &\quad then: Accept\ Bubble\ Possibility \\ &\quad else: Reject\ Bubble\ Possibility \end{aligned}$$

where the bubble velocity can be found by using the rising or the falling times and by knowing the distance between probe tips ($L$)

$$V_{r,i} = \frac{L}{\left(t2_{i,+} - t1_{i,+}\right)} \tag{8}$$

$$V_{f,i} = \frac{L}{\left(t2_{i,-} - t1_{i,-}\right)} \tag{9}$$

Assuming a flat gas/water interface in the bubble and the probe tips and interface are directly aligned with the flow, the bubble rising time velocity ($V_r$) and the bubble falling time ($V_f$) should be equivalent. In reality the probe tips are not perfectly aligned to the flow and the interface is curved, resulting in that the bubble time recorded by Probe Tip 2

was different from the bubble time recorded by Probe Tip 1. In this work we use the average of the rise time and fall time velocities as the individual bubble velocity

$$V_i = \frac{V_{r,i} + V_{f,i}}{2} \tag{10}$$

In the velocity range between the minimum and maximum accepted velocities there are accepted bubble possibilities that are undesirable. One instance of an undesirable bubble occurs when the probe breaks the free surface. The probe views this occurrence as one large bubble. This would result in unrealistic chord length distances that skew the average chord length of all the bubbles to a larger value. These surface breaks are filtered out easily enough by checking the chord length $CL_i$ or chord time $\Delta t_i$. The chord length for bubble *i* is computed from the average of the chord length obtained for Probe Tips 1 and 2 as

$$CL_i = V_i \, \Delta t_i \tag{11}$$

with the bubble chord time defined as the average of the values measured by the tips

$$\Delta t_i = \frac{\Delta t1_i + \Delta t2_i}{2} \tag{12}$$

A filter is then applied as

$$\boxed{\begin{array}{l} if: CL_{max} < CL_i \\ \quad then: Reject\ Bubble\ Possibility \\ \quad else: Accept\ Bubble\ Possibility \end{array}}$$

After filtering unacceptable bubble velocities and sizes there are still other possibilities that need to be evaluated. Fig 5a shows a situation in which two bubble events hit both probe tips very closely together in time resulting in an anomaly that can pass the previous two logical checks creating four possible bubble combinations.

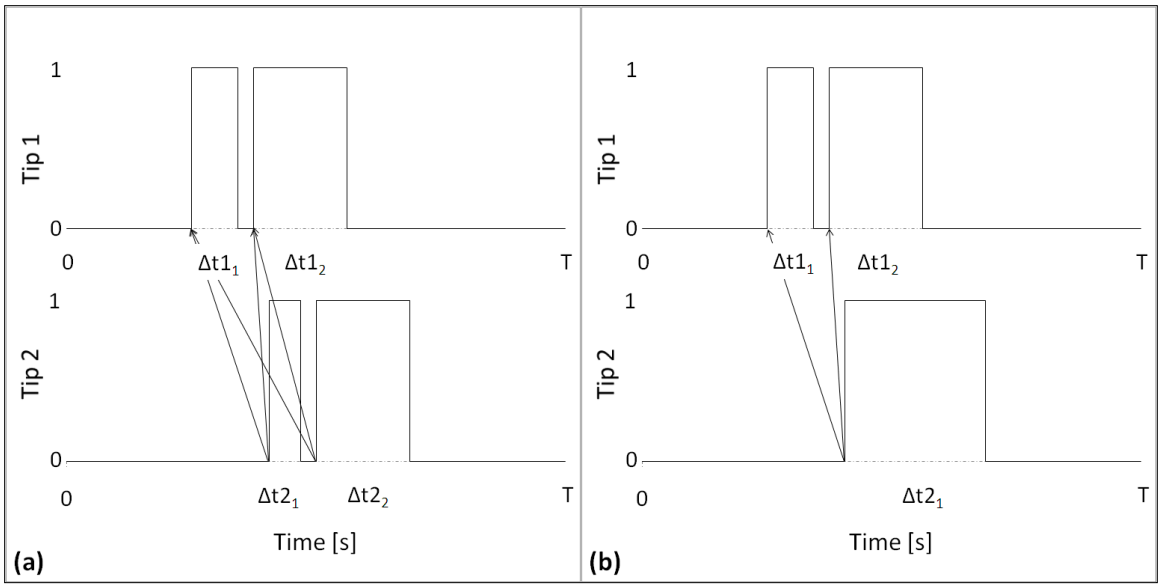


Figure 5: Indicator function events that need filtering. (a) repeated use of events resulting in four combinations, (b) repeated use of bubble events resulting in two combinations.

These situations are easy to identify because the events have to be used twice to make up the four bubble possibilities.

$$\begin{aligned} &a)\ \Delta t1_1 \sim \Delta t2_1 \\ &b)\ \Delta t1_1 \sim \Delta t2_2 \\ &c)\ \Delta t1_2 \sim \Delta t2_1 \\ &d)\ \Delta t1_2 \sim \Delta t2_2 \end{aligned} \tag{13}$$

Only two of the combinations can be chosen to eliminate the reuse of bubble events, a) and d) or b) and c). a) and d) is the correct choice, because for b) and c) to occur, the two bubbles in question would have to switch positions in the time it takes to travel between the probe tips. The assumption is made that this occurrence is unlikely so combinations are filtered to a chronological condition.

There is still one situation shown in Fig. 5b that can elude the previous three logical filters. It is the situation where there are two combinations possible due to an extra

event in one probe tip that does not get recorded in the second probe tip or vice versa. This is caused by a non perfect signal correlation. The combinations are

$$\begin{aligned} a)\ \Delta t1_1 &\sim \Delta t2_1 \\ b)\ \Delta t1_2 &\sim \Delta t2_1 \end{aligned} \tag{14}$$

In this situation the combination is selected that would have the closest velocity to the average of the previously accepted bubbles $V_{ave}$. Comparing chord times is an option but velocity measurements are much more steady than the chord time measurements so $V_{ave}$ was chosen as the velocity for the logical expression shown below

$$\boxed{\begin{aligned} &if: \left|V_{comb,a} - V_{ave}\right| < \left|V_{comb,b} - V_{ave}\right| \\ &\quad then: Accept\ Combination\ a \\ &\quad else: Accept\ Combination\ b \end{aligned}}$$

This results in an iterative process since $V_{ave}$ changes slightly after the logical loop above. With a good indicator function correlation the need for this logical loop becomes rare and most bubbles are accepted by the first three logical filters. Notice also that to avoid double-counting, once a bubble has been identified in the signals from Probe Tips 1 and 2, these bubble events are not available to pair with other events.

### 3.3. Gas Volume Fraction, Velocity, and Chord Length

The time averaged gas volume fraction for each probe can be found as while the

$$\alpha 1 = \frac{1}{T}\sum_{i=1}^{N_1}\left(\Delta t1_i\right) \tag{15}$$

$$\alpha 2 = \frac{1}{T}\sum_{i=1}^{N_2}\left(\Delta t2_i\right) \tag{16}$$

gas volume fraction filtered by out of water events is computed as in Eq. (7). Notice that the number of bubbles pierced by both probes may differ, and that the number of bubbles accepted after filtering may reject some bubbles from Probe Tip 1, 2, or both. Because Tip 1 is less intrusive than Tip 2, which is affected by Tip 1, the gas volume fraction from

Tip 1 has been used throughout the paper, either filtered as in Eq. (7) or unfiltered as in Eq. (15).

The procedure described previously provides velocity and chord length for each individual bubble. The average bubble velocity and chord length are computed as

$$\overline{V} = \frac{1}{N}\sum_{i=1}^{N} V_i \tag{17}$$

$$\overline{CL} = \frac{1}{N}\sum_{i=1}^{N} CL_i \tag{18}$$

where $N$ is the number of accepted bubbles.

### 3.4. Bubble Clouds Identification and Attribute Calculation

Visual observation at the bow clearly indicated the presence of bubble clouds formed during unsteady breaking of bow waves. The clouds can be easily recognized in the indicator functions. The average length of the clouds, along with the in-cloud bubble velocity, chord length, and gas volume fraction, are desired attributes to characterize the two-phase flow in the bow. While visual identification is easy, a standard definition of a cloud needs to be set to isolate the clouds from the indicator functions gathered from the experiments. The indicator function inside the clouds is used to compute a gas volume fraction for the cloud. A cloud is defined as a grouping of 10 or more bubbles that have rising edges separated by less than 0.75 *m*. This means that in a bubble cloud there cannot be a gap between two consecutive bubbles of more than 0.75 *m*, with this distance computed using the ship velocity $V_{ship}$. The resulting process creates a cloud indicator function, that can be used as a conditional to the indicator function to compute in-cloud properties, as shown in Fig. 6.

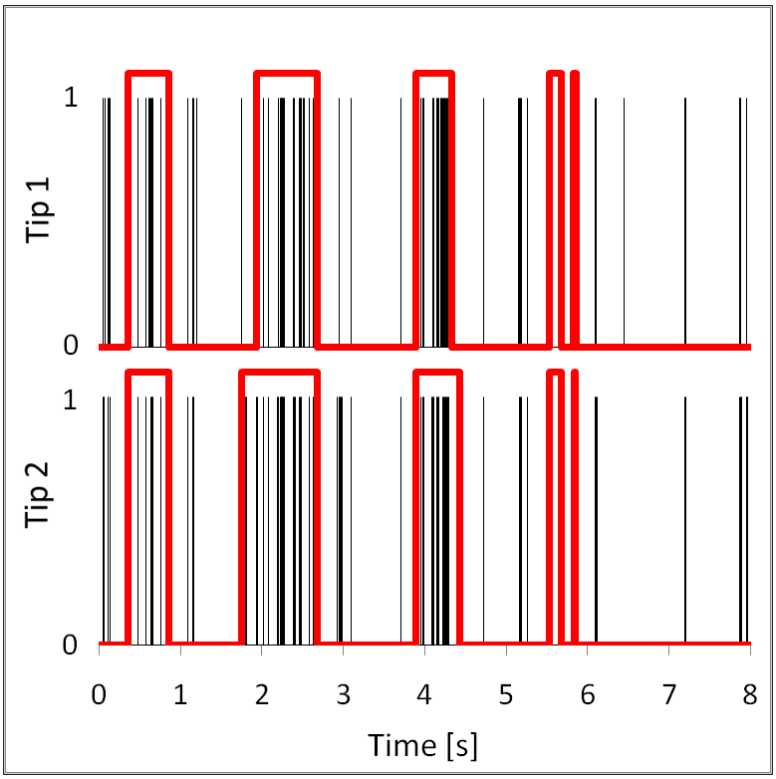


Figure 6: Indicator functions for two probe tips with the bubble clouds outlined in red by a secondary cluster indicator function. This specific data set was acquired at the bow, 0.2 *m* below the free surface with the Athena R/V traveling at 5.4 m/s (10.5 knots) using the IIHR probe.

The bubble cloud indicator function was created by the following logic

$$
\begin{aligned}
&Assume: The\ tip\ is\ in\ air \\
&if: \left(t1_{i+2} - t1_i\right) > \frac{0.75\ m}{V_{ship}} \\
&\quad then: t1_i\ to\ t1_{i+2}\ is\ in\ water \\
&\quad repeat: Step\ i\ by\ 2 \\
&if: Section_{air,i}\ contains\ < 10\ bubbles \\
&\quad then: Section_{air,i}\ is\ not\ a\ cloud\ \ \&\ \ Section_{air,i}\ is\ in\ water
\end{aligned}
$$

This expression begins with the cloud indicator function in air, and then finds the spaces between rising edges of bubbles that have a greater distance than 0.75 *m* between

them and sets that section to water. The next logical expression identifies the sections in air ($Section_{air,i}$) that do not contain at least 10 bubbles and sets that section to a value that denotes water. The remaining sections in air make up the cloud outline that creates the cloud indicator function.

The time duration of the cloud is obtained in the same way the time is calculated when a probe tip passes through an individual bubble, see Eq. (5), but by using the cloud indicator function:

$$\Delta Ct1_j = Ct1_{j-} - Ct1_{j+} \tag{19}$$

The in-cloud gas volume fraction allows for a comparison of the gas volume fraction of the cloud compared to overall time averaged gas volume fraction in Eq. (15). For cloud *j* the in-cloud gas volume fraction is

$$\alpha 1_j = \frac{1}{\Delta Ct1_j} \sum_{i=1}^{N_j} \left( \Delta t1_i \right) \tag{20}$$

The length of a cloud is defined by

$$L_j = V_{ship}\ \Delta Ct1_j \tag{21}$$

The averages of the bubble velocities and the bubble chord lengths within the clouds serve as a way to compare the bubbles in the clouds to the data sample as a whole. The average in-cloud bubble velocity and chord length are defined as

$$\overline{V}_j = \frac{1}{N_j} \sum_{i=1}^{N_j} V_i \tag{22}$$

$$\overline{CL}_j = \frac{1}{N_j} \sum_{i=1}^{N_j} CL_i \tag{23}$$

where $N_j$ is the number of bubbles in cloud *j*.

## 3.5. Bubble Size Distribution

The methodology for obtaining bubble sizes from chord length distributions coined as *unfolding* displayed herein is reported by Johansen, et al. (2010). That section on *unfolding* was contributed by Castro and is included in this thesis because it presents methodology that is integral in determining the results of this study.

A distribution of chord lengths or a chord length histogram obtained by a probe can be transformed into a distribution of bubble radii by assuming that the bubbles are spherical. The number of counts found in a certain chord length interval $(c, c+dc)$ is the combined result of the probability of hitting a bubble of diameter $D$ and the probability that the piercing of this bubble will happen with a chord length $c$. The chord lengths in this interval will be the result of a combination of several events. Some events may include hitting bubbles right through its centerline so bubble diameter is exactly equal to $c$, while other events may include piercing larger bubbles through the side such that the length traveled by the probe is still the same chord length $c$. An illustration of this scenario can be seen in Fig. 7.

The problem of finding the bubble size distribution of spheres $P(D)$ from the chord length distribution is known as *unfolding*. Classical approaches to this problem are presented in Takeo (1971), Clark and Turton (1988), Liu and Clark (1995), Liu et al. (1998) and Hu et al. (2006). The most important effect separating the chord length distribution from the size distribution is that the probe *detects* larger bubbles with more frequency than are present in the fluid just because their cross sectional area is larger. Consider a two dimensional illustration of a box with an air-water mixture in which there is a very large bubble in the center of the box surrounded by many smaller bubbles. If this box were then intersected by randomly placed lines simulating the probe path the number of times the large bubble is intersected will not be representative of the number of large bubbles in the whole volume. Another cause effecting the distributions is the finite probe

size, in which the probe is unable to detect bubbles with a diameter smaller than the probe diameter. In this regard, a model for the probe size is developed and experimental proof is presented showing that this effect cannot be neglected.

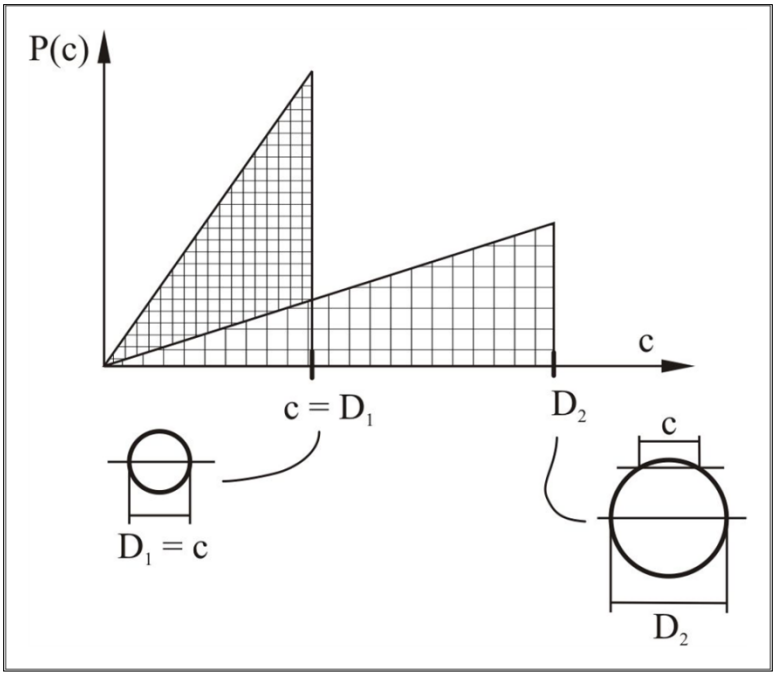


Figure 7: Counts in the chord length distribution at a certain chord length $c$ product of hitting bubbles with a diameter $D_1 = c$ and larger bubbles with diameter $D_2$.

### 3.5.1. Chord Length Distribution

The objective of the unfolding process is to find the bubble size distribution $f(D,\mathbf{x},t)$, in $bubbles/\left(m^3 \mu m\right)$. Optical probes travel along a one-dimensional trajectory providing phase information. To use this one dimensional trajectory to give us information about a three dimensional space a *3D correction* must be made. The bubble size distribution can be expressed as

$$f(D,\mathbf{x},t) = N(\mathbf{x},t)P(D,\mathbf{x},t) \tag{24}$$

where $N$ is the number density in $bubbles/m^3$ and $P(D)$ has units of $\mu m^{-1}$. The number density and gas volume fraction can be found in terms of the number density distribution as

$$N(\mathbf{x},t) = \int_0^\infty dD\, f(D,\mathbf{x},t)$$
$$\alpha(\mathbf{x},t) = \int_0^\infty dD\, \frac{\pi}{6} D^3 f(D,\mathbf{x},t) \tag{25}$$

The probability of having a chord length $c$ after impact of a spherical bubble of diameter is (Clark and Turton 1988)

$$P(c \mid D) = \frac{2c}{D^2} H(c-D) \tag{26}$$

where $H(x)$ is the Heaviside function, a step function that returns a value of zero for all negative $x$ and one for all positive $x$. Thus, a mono-dispersed size distribution measured by an optical probe results in a triangular chord length distribution. If the probe has a diameter $p$, we assume that bubbles with diameter $D$ smaller than $p$ cannot be pierced by the probe. The selection of $p$ is reasonable but somewhat arbitrary, since unquestionably high speed bubbles can be pierced by bigger probes and slower ones will resist piercing. With this model the minimum chord length that can be obtained when piercing a bubble with diameter $D$ occurs when the probe center is located at a distance $p/2$ from the bubble edge as shown in Fig. 8.

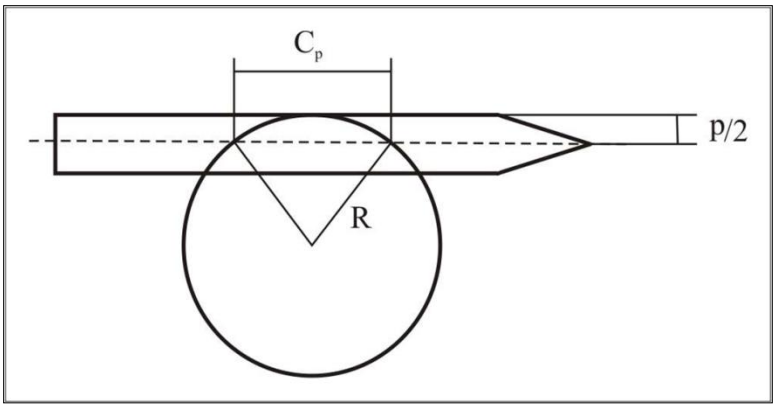


Figure 8: Situation of minimum chord size $C_p$, when the probe edge is tangent to the bubble's interface.

From a geometrical analysis this minimum chord length is

$$c_p(D) = \sqrt{p(2D-p)} \tag{27}$$

Then,

$$P_p(c \mid D) = \frac{P(c \mid D) H(c - c_p) H(D - c)}{\int_{c_p}^{D} dc P(c \mid D)} \tag{28}$$

and using Eq. (26) yields

$$P_p(c \mid D) = \frac{2c}{(D-p)^2} H\left(c - c_p(D)\right) H(D - c) \tag{29}$$

Now consider a possible probe trajectory in which it travels a distance of length $L$, as seen in Fig. 9.

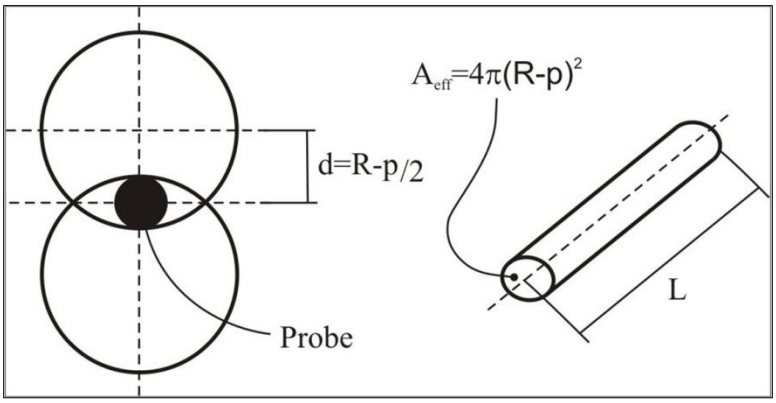


Figure 9: The probe will hit bubbles if its circumference is completely included inside the bubble cross section.

A bubble of diameter $D$ will be hit by the probe if its center is at a maximum distance $d = R - p/2$ from the probe trajectory. Therefore, the probe will only hit bubbles that are inside a tube of length $L$ and an effective cross sectional area $A_{eff} = \frac{\pi}{4}(D-p)^2$. The number of bubbles with diameter in the interval $(D, D+dD)$ inside this tube is

$$n(D)\,dD = N\,L\,A_{eff}\,P(D)dD \tag{30}$$

A fraction $P_p(c \mid D)$ of these bubbles produces counts in the chord length $c$ so that $n(D)\,dD\,P_p(c \mid D)\,dc$ is the contribution to chord lengths in chord length interval $(c, c+dc)$ from bubbles of diameters $(D, D+dD)$. Integration over all bubble sizes results in the total number of counts in $(c, c+dc)$

$$n(c) = dc\int_0^{\infty} dD\,P_p(c \mid D)\,n(D) = \int_c^{c_p^{-1}(c)} dD\,P_p(c \mid D)\,n(D) = N\,L\,\frac{\pi c}{2}\int_c^{c_p^{-1}(c)} dD\,P(D) \tag{31}$$

where $c_p^{-1}(c) = \frac{c^2 + p^2}{2p}$.

The total number of bubbles pierced by the probe can be computed by integration of Eq. (30)

$$N_h = \int_p^\infty dD\, n(D) = N\, L \int_p^\infty dD\, A_{eff}(D)\, P(D) = N\, L\, \bar{A}_{eff} \tag{32}$$

where $\bar{A}_{eff} = \int_p^\infty dD\, A_{eff}(D) P(D)$. The chord length distribution will be the quotient of the number of pierced bubbles in chord length interval $(c, c+dc)$, Eq. (31), with the total number of pierced bubbles, Eq. (32). Omitting the differential $dc$

$$\begin{aligned} P(c) &= \beta c \int_c^{c_p^{-1}(c)} dD\, P(D) \\ \beta &= \frac{\pi}{2\bar{A}_{eff}} \end{aligned} \tag{33}$$

The validity of Eq. (33) was verified by conducting simulations of synthetic probe signals obtained from a known size distribution of bubbles inside a box. This expression naturally includes the 3D correction and also provides an explicit form for the computation of the constant $\beta$. Hu et al. (2006) also considers the 3D correction and arrives at the same form of Eq. (33), but that study did not consider a finite-sized probe. Ignoring the 3D correction would lead to gross errors if the size distributions deviate significantly from mono disperse, as it is the case in experimentation and herein.

### 3.5.2. Properties of the Transformation

Before inverting Eq. (33) some properties of the transformation are analyzed. In the limit $p \to 0$ Eq. (33) reduces to

$$P(c) = \beta c \int_c^\infty dD\, P(D) \tag{34}$$

and $P(c)$ can be obtained from

$$\frac{d}{dc}\left(\frac{P(c)}{c}\right)\Bigg|_{c=D} = -\beta P(D) \tag{35}$$

In this case the inverse problem can easily be solved. However, the direct use of Eq. (35) to solve the problem involves taking the derivative of experimental data; any noise in the experimental data will result in extremely amplified noise in the inverse solution. Researchers have had difficulties in finding an inverse solution free of noise. Even if one discretizes Eq. (34) and solves a system of equations, the numerical discretization is still an approximation of the derivative in Eq. (35). Another important observation is that since $P(D)$ is a probability density function it is positive, then from Eq. (35)

$$\frac{d}{dc}\left(\frac{P(c)}{c}\right) < 0 \tag{36}$$

Eq. (36) means that $P(c)/c$ is a monotonically decreasing function of $c$. Fig. 10a shows $P(c)/c$ obtained from experimental data taken at the bow of *Athena II* R/V. We see that $P(c)/c$ is not monotonically decreasing; to produce a positive diameter distribution it should be monotonically decreasing. Similar results are obtained with any other set of the experimental data taken. The inconsistency is resolved by introducing a finite size probe. This causes $P(c)/c$ to decrease for small chord length $c$, as occurs in the experimental data. Fig. 10b shows the effect of finite size probe tip on $P(c)$ and $P(c)/c$ for an arbitrary exponentially decreasing $P(D)$. While an infinitesimally small probe shows a monotonically decreasing $P(c)/c$, a 125 μm probe tip results in a distribution much closer to that found in the experiments.

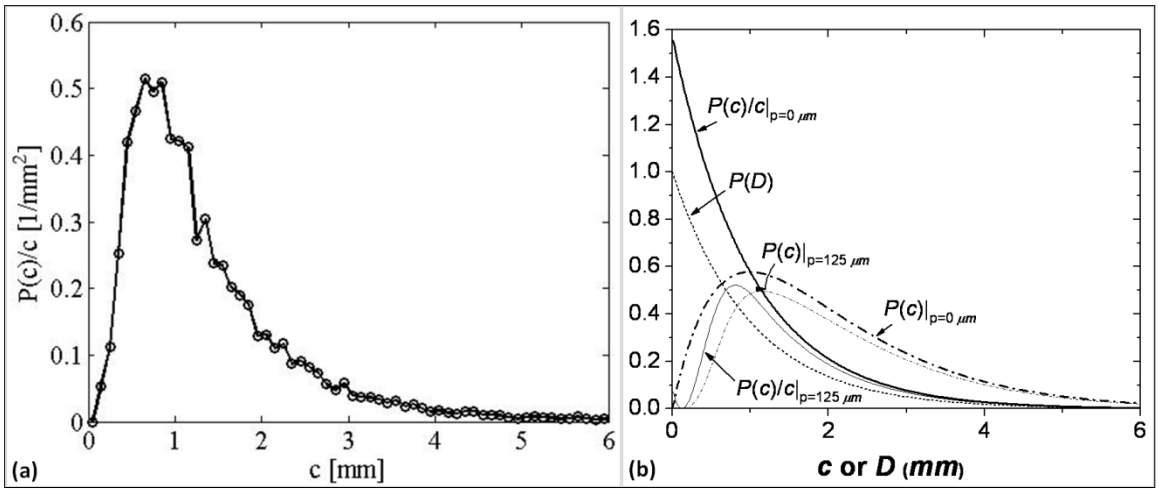


Figure 10: (a) $P(c)/c$ for data taken at the bow of Athena R/V at $z = -0.1\,m$. Note that $P(c)/c$ is not monotonically decreasing with $c$, (b) $\tilde{P}(D)$ for an arbitrary size distribution function, and corresponding $P(c)$ and $P(c)/c$ for probe tips 0 and 125 $\mu m$ in diameter.

### 3.5.3. Unfolding of the Bubble Size Distribution

The constant $\beta$ in Eq. (33) is not known *a priori*. Defining $\tilde{P}(D) = \beta P(D)$ yields

$$P(c) = c \int_{c}^{c_p^{-1}(c)} dD\, \tilde{P}(D) \tag{37}$$

The size distribution can be found by solving for $\tilde{P}(D)$ and normalizing to 1.

When performing an experiment the results are not the continuous chord size distribution $P(c)$ but a histogram that gives the number of counts in a chord length interval $\Delta c_g = c_{g+1} - c_g$. The chord size is discretized in $G_c$ intervals with $g$ going from 1 to $G_c + 1$. In order to compare with the experimental histograms we define

$$P_{cg} = \int_{c_g}^{c_{g+1}} dc\, P(c), \quad g = 1 \text{ to } G \tag{38}$$

The minimum and maximum chord sizes will be $c_1 = p$ and $c_{G_c+1} = c_{max}$ where $c_{max}$ is the maximum chord size in the experimental histogram. $P_{cg}$ and $\tilde{P}(D)$ are then related by

$$P_{cg} = F_g\left(\tilde{P}(D)\right) = \int_{c_g}^{c_{g+1}} dc\, c \int_{c}^{c_p^{-1}(c)} dD\, \tilde{P}(D) \tag{39}$$

The diameters are discretized in $G_D$ intervals. The maximum diameter is $D_{G_D+1} = D_{max}$ and the minimum diameter is $D = p$ since bubbles smaller than $p$ cannot be detected. The maximum diameter is chosen to be the maximum chord length. It is assumed that $P(D_{G_D+1}) = 0$. A piecewise linear approximation can be used for the bubble size distribution,

$$P(D) = \sum_{g=1}^{G_D} P_g \gamma_g(D) \quad \text{on} \quad (p, D_{max}) \tag{40}$$

where $\gamma_g(D)$ is the hat function

$$\gamma_g(D) = \begin{cases} \dfrac{D - D_{g-1}}{D_g - D_{g-1}} & D_{g-1} < D < D_g \\ \dfrac{D_{g+1} - D}{D_{g+1} - D_g} & D_g < D < D_{g+1} \\ 0 & \text{Otherwise} \end{cases} \tag{41}$$

In this way $P(D_g) = P_g$. Substituting Eq. (40) into Eq. (39), and since F is a linear operator yields

$$P_{cg} = \sum_{g'=1}^{G_c} P_{g'} \mathrm{F}\left(\gamma_{g'}(D)\right) \tag{42}$$

The weights $\mathrm{F}\left(\gamma_g(D)\right)$ can be computed analytically and Eq. (42) provides $G_c$ equations with $G_D$ unknowns. Typically in the experiments the number of bins in the chord length histogram, $G_c$, was around 100 and the number of unknowns was set to around eight. In order to solve this system of equations a least squares procedure was used. If the measured histogram is $P_{cg}^m$, the following norm is minimized:

$$F = \sum_{g'=1}^{G} (P_{cg'} - P_{cg'}^{m})^2 \tag{43}$$

Note that Eq. (40) provides a smooth approximation to $P(D)$. As the number of diameters $G_D$ is increased the residual in Eq. (43) goes to zero, and will be exactly zero when $G_D = G_c$, but also the noise in $P(c)$ will be gradually amplified into noise in $P(D)$. The appropriate value for $G_D$ that provides a reasonable smooth distribution with as many points as possible is found by trial and error.

## 3.6. Uncertainty Analysis

The ASME PTC 19.1-2005 Test Uncertainty Standards and Guidelines (ASME 2005) were followed in the error and uncertainty analysis. A summary of the methodology is presented initially, and then uncertainty evaluations for ship speed, probe depth, bubble velocity, chord length and gas volume fraction are presented separately. Uncertainty estimation on chord length or bubble size distributions has not been attempted.

### 3.6.1. Uncertainty assessment methodology summary

Measurement error is the difference between a measured value and its true value. The two components of this error are the random error and the systematic error. The combined standard uncertainty is

$$\mu_{\bar{x}} = \sqrt{b_{\bar{x}}^2 + s_{\bar{x}}^2} \tag{44}$$

where $b_{\bar{x}}$ is the systematic standard uncertainty and $s_{\bar{x}}$ is the random standard uncertainty,

$$b_{\bar{x}} = \sqrt{\sum_{k=1}^{K} b_{x_k}^2} \tag{45}$$

$$s_{\bar{x}} = \frac{T_{\upsilon,95}\, s_x}{\sqrt{N}} \tag{46}$$

and $\bar{x}$ represents the arithmetic mean of $N$ samples,

$$\bar{x} = \frac{1}{N}\sum_{i=1}^{N} x_i \tag{47}$$

In Eqs. (45)-(47), $b_{\bar{x}_k}$ represents elemental systematic standard uncertainties, $K$ represent the total number of elemental systematic standard uncertainties identified, $NN$ is the number of repeated measurements, $T_{\nu,95}$ is the student's $T$ value with $\nu = N-1$ the number of degrees of freedom for a 95% confidence interval, and $s_x$ represents the standard deviation,

$$s_x = \sqrt{\sum_{i=1}^{N} \frac{\left(x_i - \bar{x}\right)^2}{N-1}} \tag{48}$$

For a result $R$ calculated by an equation containing several independent parameters $\bar{X}_j$, such that $R = f\left(\bar{X}_1, \bar{X}_2, \ldots, \bar{X}_J\right)$, the uncertainty is computed using error propagation, where

$$\mu_R = \sqrt{b_R^2 + s_R^2} \tag{49}$$

with $b_R$ the systematic standard uncertainty and $s_R$ the random standard uncertainty of the result, computed as

$$b_R = \sqrt{\sum_{j=1}^{J} \left(\theta_j b_{\bar{x}_j}\right)^2} \tag{50}$$

$$s_R = \sqrt{\sum_{j=1}^{J} \left(\theta_j s_{\bar{x}_j}\right)^2} \tag{51}$$

where $b_{\bar{X}_j}$ and $s_{\bar{X}_j}$ are the systematic and random standard uncertainties, respectively computed as in Eqs. (45) and (46), and $\theta_j$ is the sensitivity coefficient of a parameter $j$,

$$\theta_j = \frac{\partial R}{\partial \bar{x}_j} \tag{52}$$

### 3.6.2. Bubble Velocity

The bubble velocity is computed from Eqs. (8)-(10), and depends on the length between probe tips $L$ and the time it takes for a bubble to cross both probes tips. The uncertainty for the velocity of one bubble is computed from the error propagation expression

$$\mu_{v_i}^{\ 2} = \left(\frac{\partial V_i}{\partial L} B_L\right)^2 + \left(\frac{\partial V_i}{\partial t} B_r\right)^2 \tag{53}$$

where $B_r$ is the time resolution error. Since the sampling rate of the data acquisition system was 1 MHz, the systematic standard resolution uncertainty is

$$B_r = \frac{Sample\ Rate}{2} = 0.5\times 10^{-6}\, seconds \tag{54}$$

The individual bubble velocity uncertainty is then

$$\mu_{v_i}^{\ 2} = \left(\frac{1}{t} B_L\right)^2 + \left(\frac{-L}{t^2} B_r\right)^2 \tag{55}$$

Using the definition of velocity in Eqs. (8)-(10), the uncertainty reduces to:

$$\mu_{V_i}^{\ 2} = \left(\frac{V_i}{L} B_L\right)^2 + \left(\frac{V_i^2}{L} B_r\right)^2 \tag{56}$$

In Eq. (56) $B_L$ was measured with a Nikon D80 camera with a resolution of $6\mu m\ per\ pixel$. From the picture there the edges of the probe tips were discernable in a distance of about two pixels.

The uncertainty in the average velocity, Eq. (17), adds a random uncertainty resulting in

$$\mu_{\bar{V}}^{\ 2} = \left(\frac{\bar{V}}{L} B_L\right)^2 + \left(\frac{\partial V_i}{\partial t} B_r\right)^2 + \left(\frac{T_{\upsilon,95}\, s_v}{\sqrt{N}}\right)^2 \tag{57}$$

In Eq. (57) $s_v$ is the standard deviation of the individual bubble velocity measurements and $N$ is the total number of bubbles measured in the trial.

### 3.6.3. Bubble Chord Length

The bubble chord length is computed from Eq. (11), and the average chord length from Eq. (18). The propagated error for the chord length is then

$$\mu_{CL}^2 = \left(\Delta t_i \, \mu_{V_i}\right)^2 + \left(V_i \, \mu_{\Delta t_i}\right)^2 \tag{58}$$

The time uncertainty $\mu_{\Delta t_i}$ has two main systematic elemental errors,

$$\mu_{\Delta t_i}^2 = B_{tp,i}^2 + B_r^2 \tag{59}$$

$B_{tp,i}$ is the uncertainty in time due to the finite penetration time of the bubble surface, and due to bubble deformation. This error is affected by the digitalization procedure (double threshold in our case) and by the probe geometry (Cartellier and Achard 1991). Herein it is conservatively assumed that most of the uncertainty is due to the finite rise time of the signal, computed from

$$B_{tp,i} = \frac{L_{p,eff}}{V_i} \tag{60}$$

where $L_{p,eff}$ is the effective active length of the probe and $V_i$ is the bubble velocity. This piercing time was used by Abuaf et al. (1978) to measure the interface velocity. The effective tip length used for the IIHR probe was 62.5 $\mu m$ and 125 $\mu m$ for the RBI probe.

To estimate the uncertainty of the average chord length, a random error is added of the form

$$s_{\overline{\Delta t}} = \frac{T_{\nu,95} \, s_{\Delta t}}{\sqrt{N}} \tag{61}$$

where $s_{\Delta t}$ is the standard deviation of all the measured time durations. The average chord length uncertainty is then estimated as

$$\mu_{\overline{CL}}^2 = \left(\overline{\Delta t} \, \mu_{\overline{V}}\right)^2 + \left(\overline{V} \, \mu_{\overline{\Delta t}}\right)^2 \tag{62}$$

where the uncertainty in the average time in air is

$$\mu_{\overline{\Delta t}}^2 = B_{tp}^2 + B_r^2 + s_{\overline{\Delta t}}^2 \tag{63}$$

where $B_{tp}$ is computed with the average velocity instead of the bubble velocity. Other errors, such as those due to partially pierced bubbles (Carrica et al. 1995), are neglected.

### 3.6.4. Gas Volume Fraction

The gas volume fraction is computed as

$$\alpha = \frac{1}{T}\sum_{i=1}^{N}\Delta t_i = \frac{N\,\overline{\Delta t}}{T} \tag{64}$$

*N* and *T* are determined with very little error, so the gas volume fraction uncertainty is

$$\mu_\alpha = \frac{N\,\mu_{\overline{\Delta t}}}{T} \tag{65}$$

where $\mu_{\overline{\Delta t}}$ is computed using Eq. (63).

### 3.6.5. Ship Speed and Probe Position

The uncertainty in ship speed was adopted based on estimation by the ship's captain. The ship speed respect to the water varied no more than 0.5 knots above or below the set velocity, resulting in an uncertainty of ±0.25 *m*/*s*. The probe location uncertainty in relation to the ship was estimated in ±0.01 *m*. The probe depth uncertainty in relation to the waterline was caused in addition by pitch, heave and roll of the ship, and wave motions, which were relatively small in the bay and near the coastline where measurements were taken. This error is estimated in ±0.025 *m* for the calm days and ±0.05 *m* for the days with more active seas.

## 3.7. Data Analysis Program Creation and Testing

A Fortran 90 program was created to analyze the raw indicator function signal produced by the RBI ISO software. This program uses the methodology presented in Section 3.1 through Section 3.4. This program was tested by a synthetic indicator function signal created by a program that inserts a double probe in a set scenario where gas volume fraction, probe speed, inserted bubble radii, and sample time are known. This program creates a synthetic signal by first creating a synthetic multiphase flow. To create the multiphase flow the program begins by making a cubic volume with dimensions specified by the user in which to seed perfectly spherical bubbles. The bubble locations are seeded by a semi-random number function in Fortran. These bubbles are then given radii to correspond with the users' specification for bubble size. The program then simulates a probe passing through this box for a certain period of time at a certain probe speed as specified by the user. The bubble analysis program is then able to analyze the synthetic signal as if it were experimental data. Table 1 below shows the comparison between a perfectly correlated synthetic signal and the output of the data analysis program that was used to analyze the data presented in the results.

Table 1: Direct comparison between synthetic signal and data analysis program output.

| | Gas Volume Fraction [%] | Probe Speed [m/s] | Inserted Bubble Radii [mm] |
|---|---|---|---|
| Synthetic Signal | 1.0000 | 5.4000 | 1.0000 |
| Data Analysis Program Output | 0.9983 | 5.4000 | 1.3335 |

The synthetic gas volume fraction was set to be one percent, with seeded bubbles of one *mm* radii, a probe speed of 5.4 *m/s* for 60 seconds. The Fortran program creates a synthetic signal assuming infinitesimally small probe tip diameter. The bubble analysis program does quite well analyzing a perfectly correlated signal. It is assumed as it is in experimentation that if the sample time was infinite the measured gas volume fraction would converge to the actual gas volume fraction of the fluid. The average bubble chord length output by the analysis program is expected to be $4/3\,r$ which is found by dividing the equation for volume of a sphere by the equation for area of a circle shown below in Eq. (66).

$$\overline{CL} = \frac{V_{cylinder} = V_{sphere}}{A_{Circle}} = \frac{4/3\,\pi r^3}{\pi r^2} = 4/3\,r \tag{66}$$

The reason this relation is accepted is because an approaching probe see's a bubble as a 2D circle with a depth, which is chord length. A 2D circle with depth is really a 3D cylinder. So by averaging the chord length it is as if we put the volume of a sphere and smashed it to the shape of a cylinder making the volume of a cylinder equivalent to that of the sphere. However, this equation only works mono-dispersed fluid where all the bubble sizes are equivalent and known.

# CHAPTER 4

# RESULTS AND DISCUSSION

Measurements were taken at the bow, masker and transom locations shown in Fig. 2. The positions are non-dimensionalized with the ship length, with the *x* axis running from bow to stern and the *y* axis pointing to starboard, with the origin on the point where the free surface and the bow intersect, also known as the forward perpendicular.

## 4.1. Measurements at the Bow

Measurements at the bow were performed using RBI II and IIHR probes on two separate days, Tuesday and Wednesday respectively. Measurements on Tuesday with the RBI II probe were performed with a more rippled sea surface, but still essentially calm, while the IIHR probe was used on Wednesday a calmer day. The first day's measurements, on Tuesday, were performed in Saint Andrews Bay due to higher winds and rougher seas. In the bay algae and other debris were suspended in the water after runoff from the previous day's rain, causing the use of the sturdier RBI II probe, as it was viewed as the sturdiest. In addition, fresh water from the rain induced slightly less salinity than normal on that day. Wednesday, the following day, conditions were much cleaner and calmer and the IIHR probe was used in the gulf. Thus probe RBI II is associated with measurements at the bay with less calm conditions and probe IIHR with measurements at the gulf with calmer conditions.

The probes were located about 3.5 *m* downstream of the bow breaking wave, which is approximately 0.284 ship lengths. It was observed that unsteady breaking of the bow wave created air entrainment during the plunging phase of the breaking, creating bubble clouds that traveled downstream as the ship maintained its velocity. The average period of this unsteady breaking at 5.4 *m*/*s* was 2.8 *s* in head waves, obtained from frequency analysis of the bubble clouds measured on the second day with the IIHR probe,

as discussed later in this section. The period of bubble cloud encounter corresponded to waves with a wavelength of 35.2 *m*. The path of the bubble clouds was more irregular in the presence of higher waves, due to less repetitive location of the breaking of the wave. As a consequence, measurements with the RBI II probe did not always cross the path of the bubble clouds. This irregularity resulted in lower gas volume fractions. In addition, lower salinity in the bay could also result in lower gas volume fractions, as reported in Jeon et al. (2008).

Fig. 11 shows average gas volume fraction, bubble velocity and chord length as a function of depth, lateral position and ship velocity, taken with the RBI II and IIHR probes. The gas volume fraction, Fig. 11a, shows significantly smaller values inside the bay, while at the same time showing larger values when running against the waves. A higher gas volume fraction while running against the wave is expected due to the more intense collisions with waves, creating more turbulence to entrain bubbles. Significant time periods with the probe out of the water occurred inside the bay for the highest probe positions, as evident from the difference between the gas volume fraction computed with the raw indicator functions and the filtered indicator function that removes the time the probe is in air. A clear decay of the gas volume fraction with depth is observed. Gas volume fractions of about 2% are observed in the gulf near the free surface, while values between 0.2% and 0.5% are observed in the bay sailing with and into the waves, respectively.

Bubble velocities, shown in Fig. 11b, are slightly faster than the ship speed of 5.4 *m*/*s*, with no significant change when sailing with or into the waves. The IIHR probe clearly shows a trend to lower velocity at deeper locations, where the effect of the water acceleration around the hull decreases. Due to the shape of the hull as the probe goes deeper the distance to the hull from the probe tip increases slightly, corroborating the hull effects on water acceleration. It can be seen in Fig. 11c that the average bubble chord

length is around 2 *mm*, with significant scattering around that value. There is also a slight but noticeable trend that deeper locations result in smaller average chord lengths, also in Fig. 11c.

In Figs. 11d, 11e and 11f the effects of ship speed at different lateral locations for measurements in the bay with probe RBI II are shown. Fig. 11d indicates that the gas volume fraction in general increases closer to the hull and with ship speed, as expected. The trend to higher gas volume fractions when sailing into the waves, already observed in Fig 11a, is repeated again in Fig. 11d for different ship speeds and lateral distances to the hull. The bubble velocity, shown in Fig. 11e, exhibits higher velocities than the ship at higher distances from the ship, but become smaller closer to the hull, indicating boundary layer effects. The probe positioned at $y = 0.0474$ is about 25 *mm* away from the hull, where accumulation of bubbles was visually observed; reaching gas volume fractions close to 1% as seen Fig. 11d. Bubble velocities farther out from the ship appear to be faster when sailing with the waves than when sailing into them, with the trend reversed near the hull. These trends are however within the errors of the measurements. In Fig. 11e the ship bubble velocities are compared to ship velocities. In general the bubble velocities are larger but at lower ship speeds the bubble velocity in the ship system decreases significantly. It can also be seen that the bubbles were moving faster when sailing into the waves as at higher ship speeds but the observed trend is reversed for lower ship speeds. The average bubble chord length with ship speed in Fig. 11f shows significant scattering in the data, not revealing a clear trend, suggesting that bubble chord length in the entrainment depth (0.1 *m* below the surface) is fairly independent of ship speed. Note that the average bubble chord length is heavily biased toward larger bubbles, since the cross section of the bubbles decreases with the radius squared. The average chord length can be viewed as a large-bubble weighted mean.

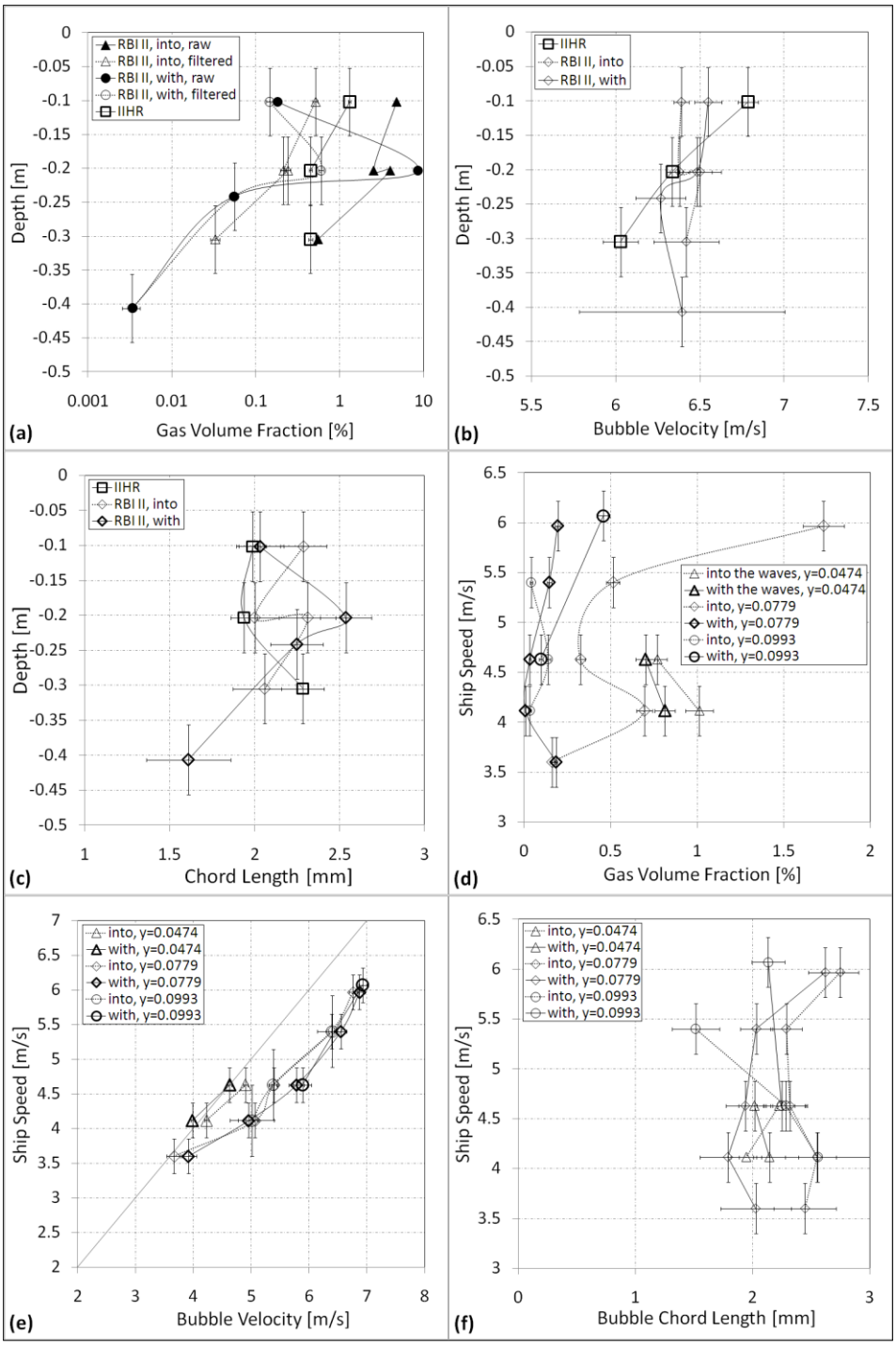


Figure 11: Measurements at the bow ($x$=0.284) and at 5.4 $m/s$ unless otherwise specified. Average gas volume fraction (a), bubble velocity (b) and chord length (c) taken with probes RBI II and IIHR at $y$=0.0779 at different depths. Average gas volume fraction (d), bubble velocity (e) and chord length (f) taken with probe RBI II at 0.1 m below the surface and several ship speeds and distances to the hull.

The RBI II probe stopped working after one of the sapphire tips was chipped by debris. The chip can be observed in Fig. 3b.

Figs. 12a and 12b show distributions of bubble velocity and chord length at three depths, from data taken with the IIHR probe at 5.4 *m/s*. The IIHR probe results had a much better correlation of the signals between tips than the RBI II probe, which resulted in a better repeatability and consistency of results. The bubble velocity shows a standard deviation respect to the average in the order of ± 0.5 *m/s* at 0.1 *m* and 0.2 *m* below the surface, due to turbulent fluctuations and vibrations in the positioning pole. The velocity fluctuations increased significantly at a depth of 0.3 *m,* likely caused by a noticeable increase in the vibrations of the pole due to a drag increase. The vibrations of the pole should not affect the average value of the velocity. The chord length distributions have similar shapes at all depths, showing a trend toward larger chord lengths at the deepest position, as already reported in Fig. 11c. It is important to note that although large chord lengths are possible, the maximum probability is for chord lengths of about 1 *mm, and* slightly smaller for deeper depths. The average chord length reported in Fig. 11c is about double that of the most probable chord length. This is due to the left hand skewed distribution and the aforementioned large cross sectional area of large bubbles.

A histogram of the length of the bubble clouds is presented in Fig. 12c. Most probable cloud lengths range from 0.5 to 3 *m* in length, with some reaching 5 *m* or more. The statistics are relatively poor since only a few hundred bubble clouds are measured in total, reflecting in the noise observed in the distributions. Figs. 12d-12f show the distributions of average velocity, average chord length and gas volume fraction within each bubble cloud. The average bubble velocity in the clouds tends to decrease with depth, while the chord length tends to increase shown in Figs. 12d and 12e respectively.

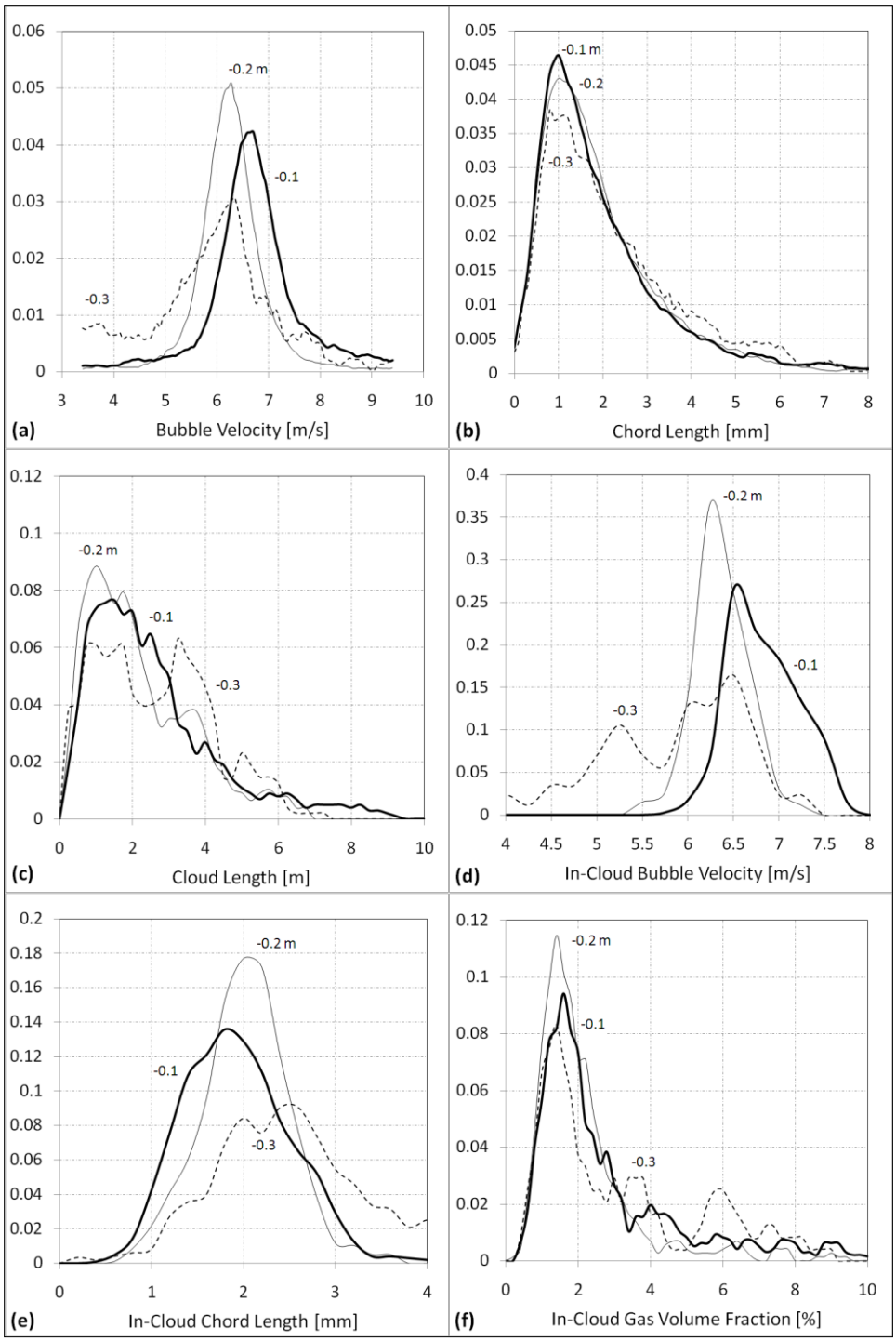


Figure 12: Bow results with the IIHR probe as a function of depth taken at $x$=0.284, $y$=0.0779. (a) bubble velocity distribution, (b) chord length distribution, (c) bubble cloud length distribution, (d) normalized histogram of the average bubble velocity in each bubble cloud, (e) normalized histogram of the average chord length within each bubble cloud, (f) normalized histogram of the average void fraction of each bubble cloud.

The same trend was observed for all bubbles in Figs. 12a and 12b. The average gas volume fraction inside the clouds shows values ranging 0.5% to 3.5%, peaking around 1.5% and with some clouds carrying as much as 6% at 0.3 *m* depth. Compare these values with the averaged gas volume fraction overall (inside and outside the clouds) shown in Fig. 11a of 1.5% closest to the free surface and 0.7% at the two deeper locations. The much lower averages indicate that most of the bubbles are located inside the bubble clouds.

Fig. 13a shows the frequency spectrum of the gas volume fraction, obtained by integrating the indicator function during a moving window of time *T*

$$\alpha(\mathbf{r},t)=\frac{1}{T}\int_{t}^{t+T}\chi(\mathbf{r},\tau)\,d\tau \qquad (67)$$

0.5 *s* was adopted for the integration time *T*. This function indicates the probability of finding a bubble during the integration time, and will respond to fluctuations slower than about half the integration period. Fig. 13a clearly indicates a peak response at about 0.33 *Hz* and harmonics of that frequency, indicating that the dominant period of encounter of the bubble clouds with the probe was about 3 *s*.

Fig. 13b shows the bubble size distributions measured at three depths that were *unfolded* from the chord length distributions as previously described. Since the procedure requires large statistics to provide smooth curves, the number of points resolved was limited to nine for the two upper depths and six for the lower position. The results show that the size distributions follow essentially the same curve, scaled with the total gas volume fraction. The probe is not small enough to capture the peak in size distribution, which includes processed sizes up to 62.5 $\mu m$ in radius. Using a photographic method in a different location and under different operational conditions, Terrill et al. (2005) found a peak for bubbles as small as 15 $\mu m$ in radius. Unfortunately photographic methods fail for large gas volume fractions, perhaps larger than 0.1%, because of shielding between

bubbles. To capture bubbles smaller than 15 $\mu m$ in radius with phase-detection probes, a tip of effective diameter of 15 $\mu m$ or less would be needed.

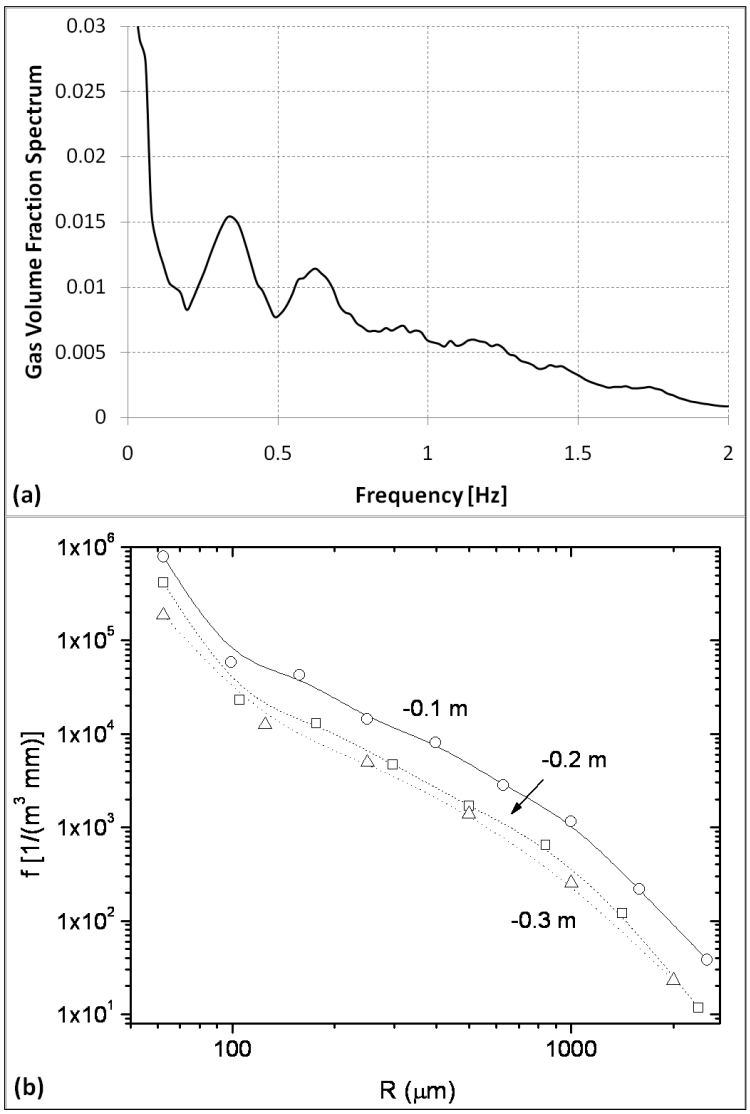


Figure 13: Bow results with the IIHR probe as a function of depth taken at $x$=0.284, $y$=0.0779. (a) frequency spectrum of the gas volume fraction at depth 0.2 $m$, showing a peak at a period of about 0.33 $Hz$, (b) bubble size distribution of all bubbles measured at each depth.

## 4.2. Measurements at the Masker

Measurements behind the masker were performed in the gulf with the RBI probe. The masker works by inducing a strong low pressure downstream of a semi-cylindrical ring that wraps around the hull, causing strong air entrainment as seen in Fig. 1. The masker induces an unsteady breaking wave running with a very sharp angle respect to the ship axis. The measurements were taken at $x = 0.487$ and at three distances from the hull. Fig. 14a shows the gas volume fraction at different speeds and lateral distances from the hull, as a function of depth. The gas volume fractions are much higher than those measured at the bow, with values reaching 5% or higher. Also worth noticing is the high variability in location of the free surface, which causes large differences between the raw and filtered signals. It is important to recall that the filter removes the effects of the probe outside of the water. There are differences between the raw and filtered signals even at depths as deep as 0.4 *m*, indicating that the masker is sucking air in by forming a deep, unsteady depression in the free surface in the form of a whirlpool. The trends of increasing gas volume fractions with speed and proximity to the free surface are clear in Fig. 14a.

The average bubble velocity, illustrated in Fig. 14b, shows that the bubbles move slightly slower than the ship near the free surface, and that the bubble velocity increases significantly at higher depths and farther out from the hull. The reasons for the bubble velocity increases are unknown and require further investigation, but a possible cause could be the formation of a large separation region downstream of the masker.

Figs. 14c and 14d show the average chord length and chord length distributions, respectively. A decrease in chord length with depth is apparent, a trend shown both by the average value as well as in the distributions. The chord lengths are comparable to those measured in the bow, averaging around 2 *mm*.

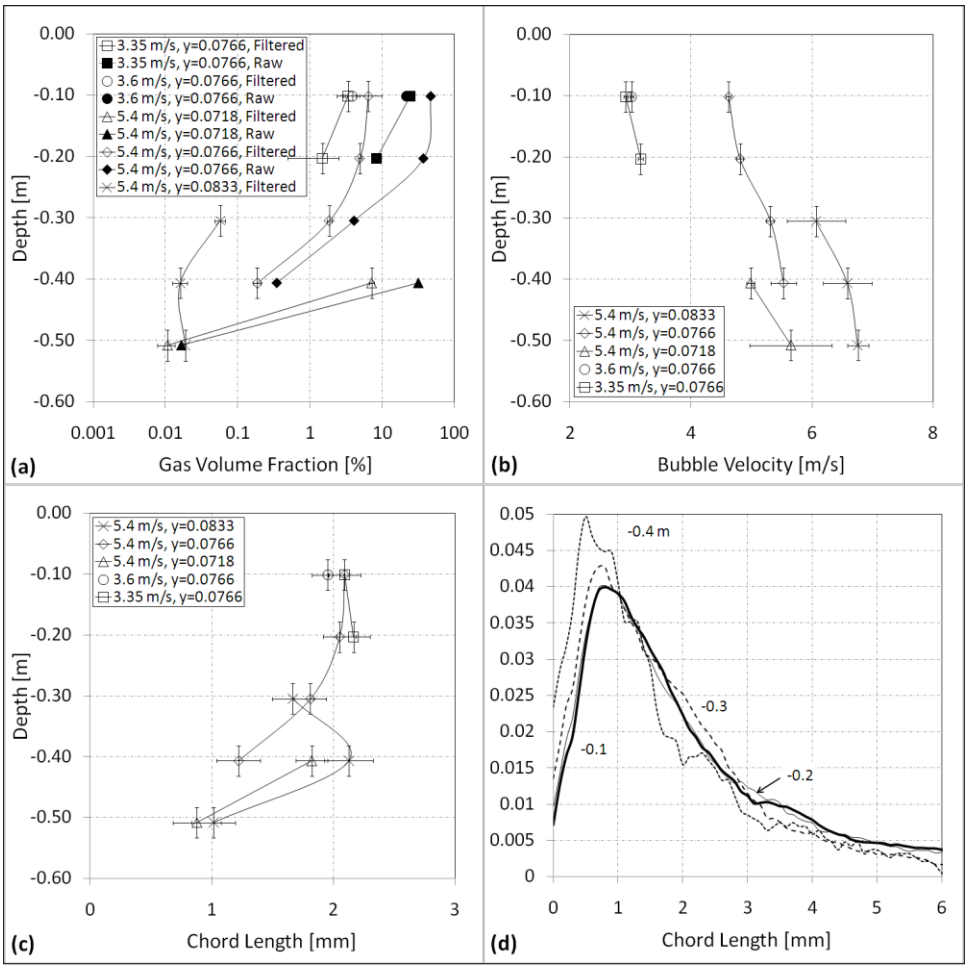


Figure 14: Results with the RBI probe downstream of the masker at $x$=0.487. (a) gas volume fraction for different probe locations and ship speeds. (b) average bubble velocity for different probe locations and ship speeds. (c) average bubble chord length measurements for different probe locations and ship speeds. (d) chord length distribution at $y$=0.0766 and 5.4 *m*/*s*.

Bubble size distributions at a location of $x = 0.487$, $y$=0.0766 ship lengths at 5.4 *m*/*s* for four depths is shown in Fig. 15. The slope of the curves drops slower than those at the bow, indicating the presence of larger bubbles. Also, as opposed to the bow, the distribution increases more gently for smaller bubbles, showing that there are a relatively smaller amount of very small bubbles. In summary there are relatively more large bubbles and fewer smaller bubbles than at the bow. These differences are likely due to

the different air entrainment processes in the bow and in the masker, where the presence of the low pressure region in the whirlpool submerges large amounts of big bubbles.

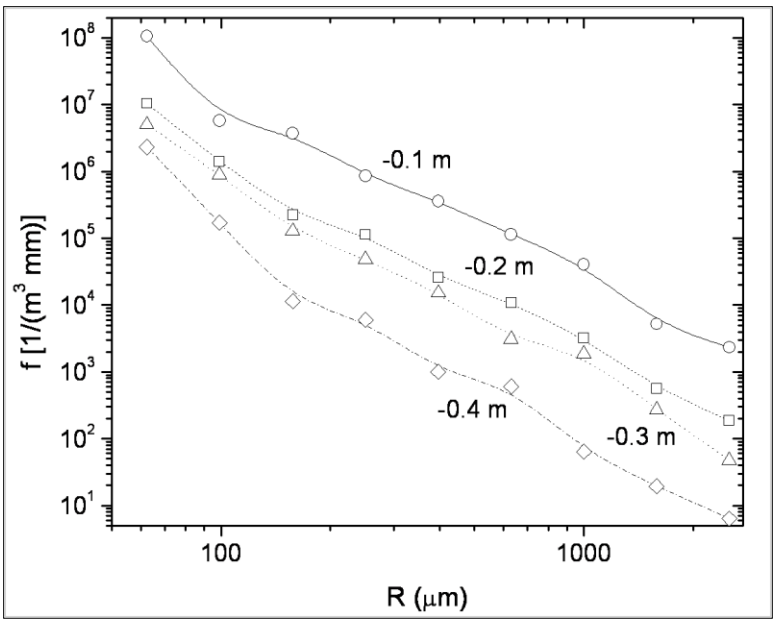


Figure 15: Bubble size distribution downstream of the masker at $x$=0.487, $y$=0.0766 and 5.4 $m/s$.

## 4.3. Measurements at the Stern

The stern flow of *Athena II* at low speeds is characterized by a wet transom with a consequent highly ventilated, unsteady roller. The depression left by the ship is overcome by the speed of the leveling wall of water before the ship transom leaves the depression. The air/water mixture that is near the free surface flows forward toward the ship and below the high-speed flow coming from the propellers that pushes the water downstream at a high speed. The combination of these flows creates the unsteady roller. The probes are designed to face the direction of the flow, tip first. From the free surface to -0.6 *m* below the free surface the probe was facing aft. The probe direction was inverted for

positions -0.6 *m* below pointing foreword. The -0.6 *m* and -0.7 *m* positions were measured with the probe pointing forward and aft.

Measurements were taken with the RBI probe at 4.6 *m*/*s* (9 knots) at two axial positions, $x = 1.0173$ and $x = 1.0038$, corresponding to the probe pointing to the stern and to the bow, respectively. The lateral location was $y = -0.021$.

The highly ventilated and unsteady nature of the transom flow makes it difficult to identify the location of the free surface, since the upper air/water mixture is composed by a frothy combination of large bubbles and drops that jumps up and down with an amplitude of over 0.3 *m*. This is clearly exposed by inspecting Fig. 16a, where at the top location the unfiltered gas volume fraction of 60% decreases to 13% after eliminating the time the probe is above the surface. This difference between unfiltered and filtered gas volume fraction decreases with depth to about zero at $z = -0.5\,m$, where the flow becomes bubbly and the free surface does not ever dip below the probe depth. At approximately $z = -0.55\,m$ the velocity reverses direction and measurements are taken with the probe pointing to the bow as seen Fig. 16b. It is important to note that aiming the probe to stern or bow changes the axial position of the probe by 0.63 *m* due to the length of the probe. Higher gas volume fractions are observed near the hull for the same depth. A change in trend is observed below the roller, where the slope in the log-linear gas volume fraction plot in Fig. 16a increases.

Fig. 16a also includes the gas volume fraction profile versus depth at 4.6 m/s (9 knots) taken with twelve conductivity probes data provided by Terrill et al. (2005). There are several important differences that make direct quantitative comparison of the gas volume fraction measurements inappropriate between the conductivity probe and optical two phase probe. The location of measurement of the conductivity probe data was taken at the centerline, approximately one meter starboard and 0.2 meters aft of the optical probe measurement location. The conductivity probes were used on the *Athena R/V I*

which is the sister ship to the *Athena R/V II*, which is worth noting but is not viewed as a significant difference in the experimental environment. The conductivity probes data was gathered in May 17$^{th}$ through the 21$^{st}$, nearly a month later than the optical data was taken, which may have caused changes in water temperature and salinity. Water temperature and salinity are both important factors that affect the conductivity of the water. The conductivity probe measurements above -0.55 meters may have had flow effects that altered the gas volume fraction due the reverse in flow direction causing the water to collide with the large positioning strut before measurement with the conductivity probes themselves. In addition, it is known that integrated conductivity probes incur in large errors at low gas volume fractions, where the change in conductivity caused by the bubbles is in the order of the change caused by salinity. Without the provision of error bars the uncertainty of the conductivity probes and the analysis method is also unknown. However, the conductivity probe data can be used to qualitatively compare the trends observed by the optical probe data. It can be seen that the gas volume fraction in the region above depth -0.55 meters decreases slowly with depth. Whereas, below -0.55 meters the gas volume fraction decreases rapidly. Without a direct comparison in measurement location and experimental conditions it is difficult to hypothesize on causes for differences in results.

The bubble velocity plot, shown in Fig. 16b, indicates that the bubbles inside the roller moves toward the bow at a fairly uniform velocity of about -1.5 *m*/*s*, and that after reversing to point downstream the velocity quickly increases to the free stream velocity. Effects of the high-speed wake of the propeller were not observed at this depth, and can be expected about 0.2 *m* deeper than measured. Detectable bubbles became rare at this position therefore it is possible that at deeper depths much longer time periods would be needed to encounter enough bubbles to get an accurate reading.

Fig. 16c shows the average bubble chord lengths as a function of depth. Below the point of water velocity direction reversal the chord lengths measured with probe pointing to the bow are more reliable because measurements were taken with the probe orientation under design conditions. The results for the probe aiming to stern located at $x = 1.0173$ are also shown. The considerable decrease in average chord length from over 1.5 *mm* at the top to below 0.5 *mm* at the deepest locations is notable.

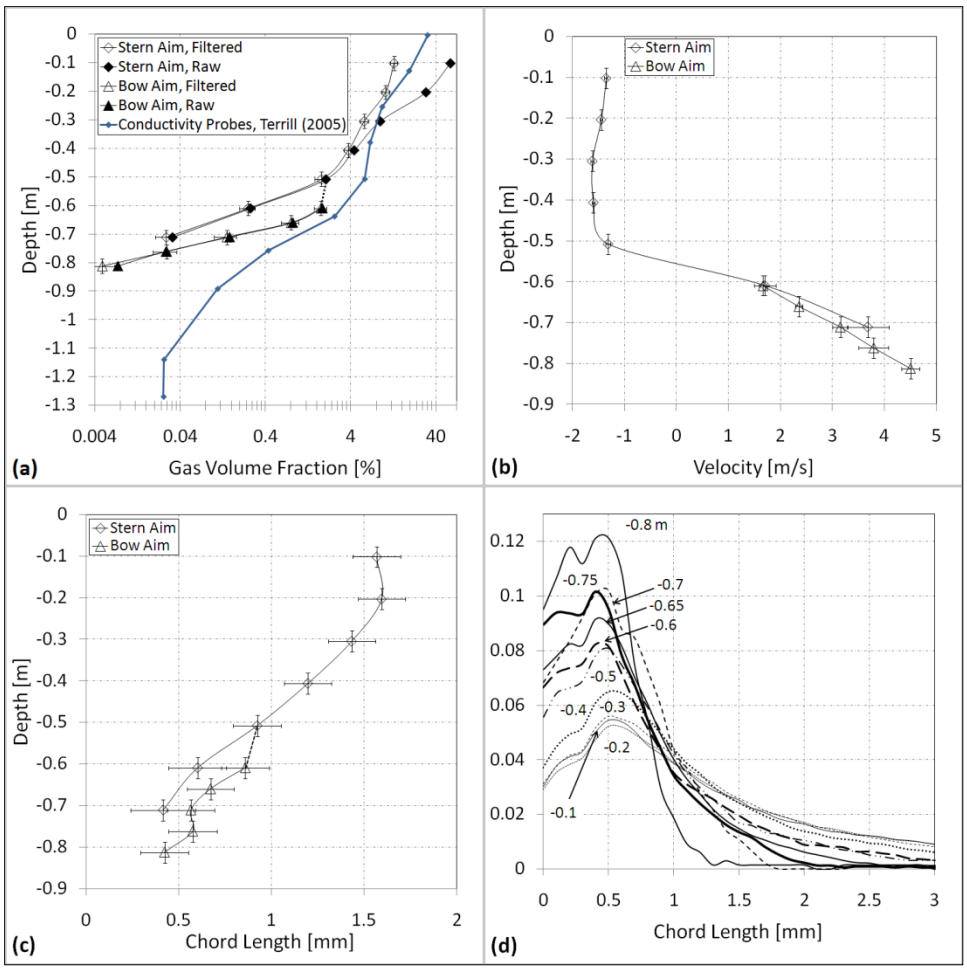


Figure 16: Stern measurements taken the RBI probe at 4.6 *m/s* (9 knots). (a) raw and filtered gas volume fraction with conductivity probe experimental data provided by (Terrill et al. 2005). (b) Average bubble velocity. (c) Average bubble chord length. (d) Bubble chord length distribution.

The trend of smaller bubbles at higher depths is reflected in the chord length distributions shown in Fig. 16d, where normalized chord length distributions are shown for depths from $z = -0.1\,m$ to $z = -0.8\,m$, with the probe always oriented against the flow. The chord length distributions need to be normalized due differences in the number of bubbles collected at different depths. Chord length distributions are essentially uniform for the shallowest three depths in Fig. 16d, showing the essentially uniform structure of the two-phase mixture in the roller. Deeper into the flow the distribution moves to smaller chord lengths, tending to show a bimodal distribution for the deeper locations. The resulting bubble size distributions that were *unfolded* from chord length distributions are shown in Fig. 17.

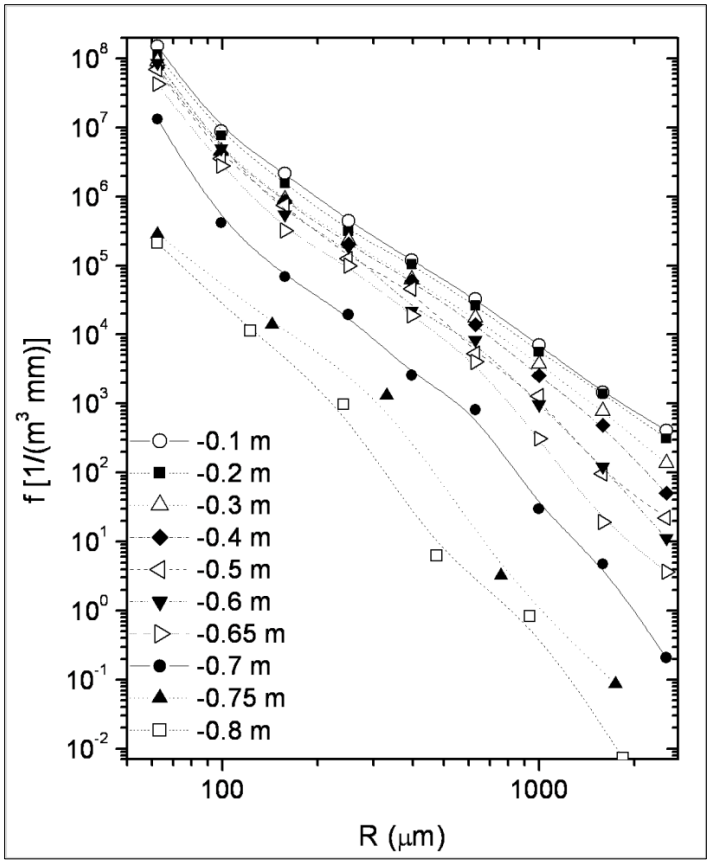


Figure 17: Bubble size distribution at the stern, taken the RBI probe at 4.6 *m/s* (9 knots).

To better visualize the shift from bubbles of large to small size as depth increases, the normalized group gas volume fractions are shown in Fig. 18a. The group gas volume fraction for a group of bubble sizes *g* is defined as (Carrica et al. 1999)

$$\alpha_g = \int_{r_{g-1/2}}^{r_{g+1/2}} f(r)\frac{4}{3}\pi r^3 dr \qquad (68)$$

where the group *g* spans from $r_{g-1/2}$ to $r_{g+1/2}$, each of these defined as the radii in Fig. 18a, starting in zero and ending in 5 *mm*, with distribution functions zero at these two extremes and assumed to change linearly between zero and the first computed radius and the largest computed radius and 5 *mm*. To produce Fig. 18a the sum of the gas volume fraction of all groups is normalized to one.

Consistent with Figs. 16d and 17, the gas volume fraction for the first three depths in Fig. 18a are dominated by very large bubbles (about 2 *mm* in radius), with almost identical distribution of gas volume fraction across the groups. As the measurements are taken deeper, the gas volume fraction distribution becomes bimodal, with the peak for the large bubbles shifting to smaller sizes of about 500 $\mu m$ for the deepest position, and developing a peak at a much smaller size about 80 $\mu m$, which for the deepest position accounts for almost 20% of the gas volume fraction. These results imply that at the deepest location the ratio of bubble number densities between bubbles smaller than 200 $\mu m$ and bubbles bigger than 200 $\mu m$ is over 10 times larger than the same ratio at the top three positions.

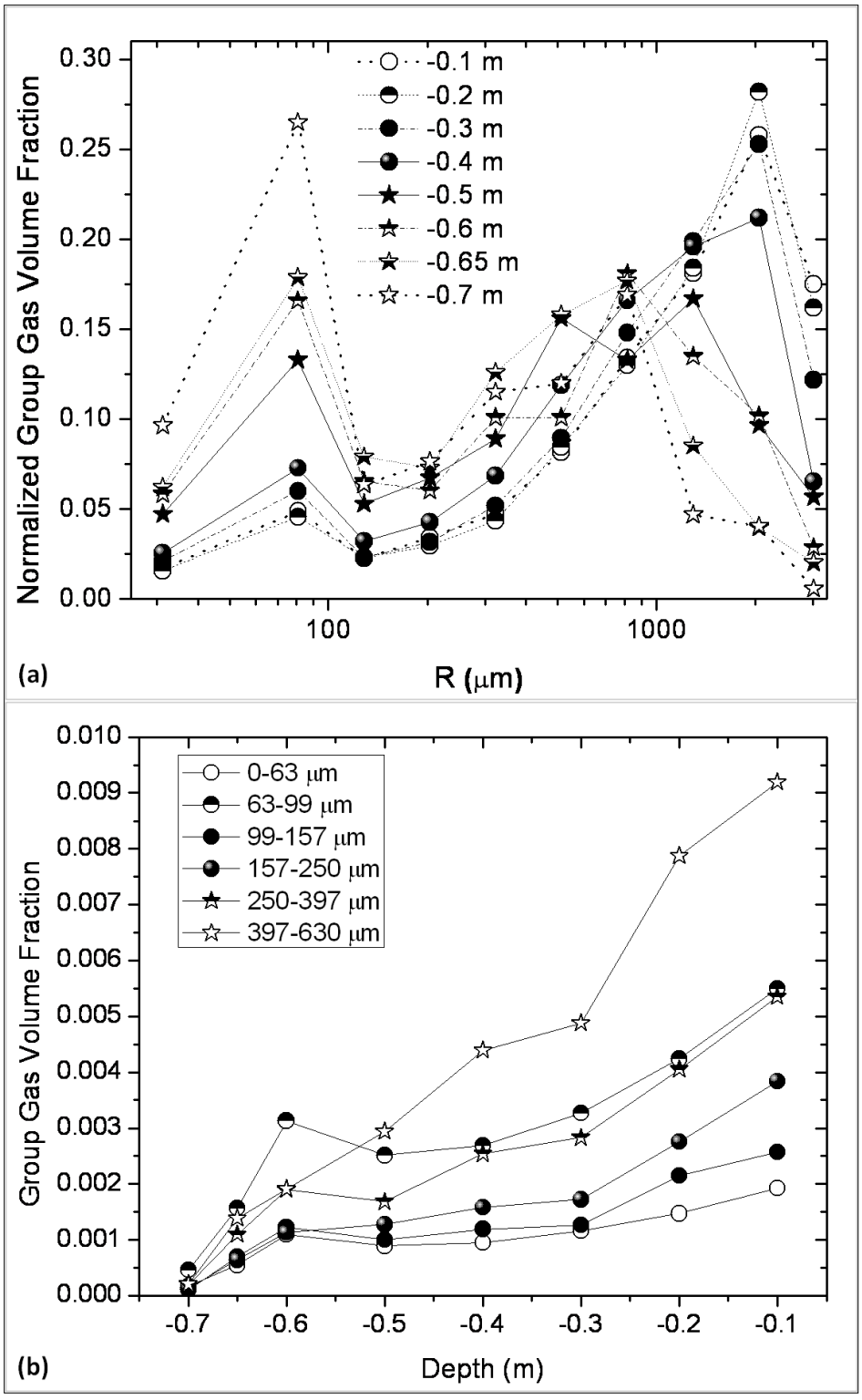


Figure 18: (a) Normalized group gas volume fraction obtained from the bubble size distributions in Fig. 17, (b) absolute group gas volume fraction profiles for the six smallest group sizes.

There are several processes that could be responsible for the relative increase of small bubbles at deeper locations, and it is of interest to identify the relative importance of each of these processes. The first effect that could account for an increase of smaller bubbles is the hydrostatic pressure increase with depth. The pressure increase will compress the bubbles and reduce their size and consequently the bubble size distribution and gas volume fraction. For our measurements this effect will result in a change in volume of only 8% at the deepest measurement position, or a change in radius of only 2.6%. Another effect of importance could be turbulent transport of bubbles from the entrainment region in the roller to deeper regions of the flow. Larger bubbles, with higher buoyancy and vertical velocity, are harder to retain deep into the flow, and thus their number density would be lower than smaller bubbles. Though this hypothesis cannot be discarded off-hand, the velocities involved in the stern flow as seen in Fig. 16b are much larger than the terminal rise velocities of the bubbles. Even the largest terminal velocity that can probably rise at about 0.3 m/s (Clift et al. 1978) is smaller than all the flow velocities seen in Fig. 16b. Thus it can be expected that bubbles transported by turbulent diffusion near the transom should not have drastically different bubble size distributions. In addition, the bubble velocity is very large at the deepest positions, suggesting that bubbles carried deep into the flow by turbulent diffusion will be transported out quickly, leaving little time for the large bubbles to rise and leave the deeper locations faster than the smaller ones. At least two other processes could be responsible for the presence of smaller bubbles at depth: the bubbles are entrained somewhere else and transported downstream to the stern, or they were generated by the propeller.

In the first hypothesis, bubbles entrained in the bow breaking wave, masker region and along the contact line between the hull and the free surface can be transported below the hull where they are subject to large shear stress and intense potential breakup, leading to small bubbles finally reaching the stern. These bubbles are present in Fig. 18b,

which shows the absolute group gas volume fraction of different sizes as a function of depth. An increase in the gas volume fraction of the smallest bubbles is observed at -0.6 *m*, where the velocity changes sign at the bottom corner of the transom stern, see Fig. 16b. Though other possibilities could be entertained, this increase in the gas volume fraction of small bubbles can be seen as evidence that bubbles are being transported from upstream below the hull. This increase in gas volume fraction of small bubbles could also be caused by local breakup of bigger bubbles into smaller ones, though the process leading to that breakup is not evident.

Small air bubbles can be generated from small nuclei that grow by absorbing air dissolved in the water in low pressure regions near the propellers. This process has been tested numerically (Hsiao et al. 2006) and proven to result in a significant number of small bubbles, but never tested in the field.

A series of experiments were performed in which several speeds were tested using the IIHR probe with the objective of evaluating the hypothesis that bubbles are produced by the propellers. The measurements were performed on a different day with slightly higher waves than the previously presented stern results. On this day the experiments carried out went with and against the waves, and each propeller was used for propulsion independently. During these measurements the downstream tip of the IIHR probe stopped working due to a faulty splice between glass and sapphire caused by excessive vibration. The broken splice prevented computations of bubble velocities and size distribution, but gas volume fraction computations were still valid using the forward tip, which was the tip with the good splice. The position of the tip was $x = 1.0065$ aiming to the bow, $y = -0.021$.

Figure 19 shows the results for ship speeds of 5.4 *m*/*s*, 4.6 *m*/*s* and 3.5 *m*/*s* (10.5, 9 and 6.8 knots). The gas volume fraction at depths closer to the free surface shows a significant increase when sailing against the waves. The values that correspond to the

ship traveling with the waves are similar to the calm water results shown in Fig. 16a. This trend could be an indication of increased number of bubbles entrained due to wave breaking and other free surface disturbances at the bow, masker and contact line that travel under the hull to resurface at the stern. Recall that the entrainment at the bow wave showed a considerable increase when sailing against the waves. These results would support the first hypothesis described previously. However, with limited information no definitive conclusion is possible.

Measurements at a single depth were also performed for the ship propelled using either the port propeller, which was directly upstream from the probe, or the starboard propeller. The operational conditions running with a single propeller change in that the rudders have to compensate to maintain the heading. In addition, the maximum speed achievable was only 3.5 *m/s* (6.8 knots) with the diesel engine running at full power. Fig. 19 shows that the gas volume fraction increases dramatically with the ship sailing only with the propeller from port, the probe side. When this ship is given propulsion from either the starboard, or the port propellers, the ship speed and heading are identical. It is reasonable to expect that bubbles entrained upstream of the propeller will not be affected by which propeller is used. This seems to indicate that the propellers are effectively generating bubbles that are detected in the stern. These results are, however, inconclusive because the propeller may instead be increasing the turbulence and air entrainment in the transom flow itself, reflecting in the gas volume fraction. Measuring at a deeper depth, in which bubbles entrained by the transom flow are unlikely to reach the probe tip, resulted in the positioning pole being bent out of shape and rendering it inoperable for any further testing.

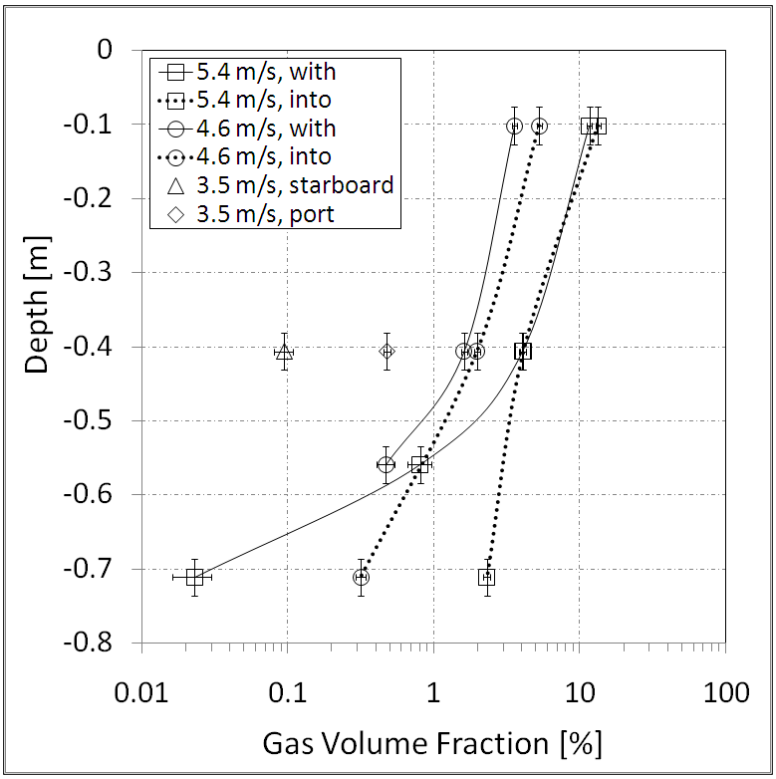


Figure 19: Stern measurements taken the IIHR probe at several speeds.

# CHAPTER 5

# CONCLUSIONS AND RECCOMENDATIONS FOR FUTURE WORK

## 5.1. Conclusions

Full-scale two-phase flow measurements at the bow breaking wave, masker and stern of the research vessel *Athena II* operating in Saint Andrew Bay and the gulf coast near Panama City, FL, were presented. The data was taken with sapphire optical probes, and processed extensively to obtain gas volume fraction, bubble velocity and bubble size distribution. To obtain the bubble size distribution a novel methodology was introduced, which accounts for the finite size of the probe.

Results at the bow show bubble clouds created by unsteady breaking of the bow wave. Average bubble velocities are slightly larger than the ship speed, caused by acceleration around the hull, and decreasing inside the boundary layer. The bubble clouds have a frequency of about 0.33 *Hz*, reflecting the encounter frequency of the waves with the ship. In general gas volume fraction was found to increase with ship speed and traveling into the waves as opposed to with the waves. Gas volume fraction was also found to decrease with depth. While typical gas volume fractions ranged from 0.1% to 1%, in-cloud gas volume fraction ranged from 1% to 8%. The bubble size distribution exposed a fairly uniform distribution for all depths measured.

Measurements at the masker revealed a highly ventilated and unsteady behavior, with gas volume fractions inside the water well over 1% near the surface. The bubble velocities were found to increase with depth and lateral distance from the hull. The size distribution shows that near the surface a much larger percentage of big bubbles with respect to total number of bubbles were found compared to deeper locations.

The presence of the roller found at the stern at low Froude numbers was detected through direct measurement of the bubble velocity. The frothy flow on the top 0.3 *m* of

the transom flow was measured and characterized, showing very high gas volume fractions that rapidly decay with depth. The average chord length also decays rapidly with depth, to almost 1/4 of the average chord length measured inside the frothy top. The chord length and bubble size distributions show that bubbles smaller than 500 $\mu m$ in radius dominate the deeper regions while larger bubbles about 2000 $\mu m$ in radius make up most of the gas volume fraction on top. Evidence was found showing that the number of small bubbles increases near the bottom edge of the transom stern, suggesting that bubbles slipping below the hull enter the transom flow in the edge. Attempts to measure the presence of bubbles created by the propeller tend to show higher gas volume fraction when the propeller directly upstream of the probe was operated, but these results were inconclusive.

## 5.2. Recommendations for Future Work

Future work is focused on the development of smaller probes of radii less than 30 $\mu m$ including both tips and designing a high strength low drag positioning system to measure directly downstream of the propellers and inside the boundary layer below the hull. The gas volume profiles at the positions measured are currently being used to create and validate the CFDShip-Iowa code as well. More features are currently being added onto the data analysis program to compute velocity by cross correlation and analyze data from a glass four-tipped optical probe.

# REFERENCES


Abuaf N., Jones O.C. and Zimmer G.A. 1978. Optical Probe for Local Void Fraction and Interface Velocity Measurements. *Rev. Sci. Instrum*. **49**, 1090–1094.

ASME, (2005), "Test Uncertainty," ASME PTC 19.1-2005, The American Society of Mechanical Engineers, 102 pp.

Barrau E., Rivière N., Poupot Ch. and Cartellier, A. 1999. Single and Double Optical Probes in Air-Water Two-Phase Flows: Real-Time Signal Processing and Sensor Performance. *Int. J. Multiphase Flow* **25**, 229-256.

Borowski, B., Sutin, A., Roh, H.S. and Bunin, B., 2008, Passive acoustic threat detection in estuarine environments. *Proc. SPIE 6945, 694513*.

Carrica P.M., Bonetto F., Drew D. and Lahey R.T. Jr. 1998. The Interaction of Background Ocean Air Bubbles with a Surface Ship. *Int. J. Num. Meth. Fluids* **28**, 571-600.

Carrica P.M., Bonetto F., Drew D. and Lahey R.T. Jr. 1999. A Polydisperse Model for Bubbly Two-Phase Flow Around a Surface Ship. *Int. J. Multiphase Flow* **25**, 257-305.

Carrica P.M., Sanz D., Delgadino G., Zanette D. and Di Marco, P. 1995. A Contribution to Uncertainties Estimation of Local Void Fraction Measurements in Gas-Liquid Flows. *Int. Symp. Two-Phase Flow Modeling and Experimentation*, Rome, Italy.

Cartellier A. and Achard J.L. 1991. Local Phase Detection Probes in Fluid/Fluid Two-Phase Flows. *Rev. Sci. Instrum*. **62**, 279-303.

Cartmill J.W. and Su M.Y. 1993. Bubble Size Distribution Under Saltwater and Freshwater Breaking Waves. *Dyn. Atmos. Oceans* **20**, 25-31.

Caruthers J., Gilbert K., Stanic S. 2009. Underwater Acoustics and Acoustical Oceanography: Session in Honor of Ralph Goodman and His Contributions to the Acoustics of Bubbles and Other Works. *157th Meeting of the Acoustical Society of America*. Portland, OR.

Clark N.N., Turton R. 1988. Chord Length Distributions Related to Bubble Size Distributions in Multiphase Flows. *Int. J. Multiphase Flow* **14**, 413-424.

Clift R., Grace J., Weber M. 1978. *Bubbles, Drops and Particles*. Dover, Mineola, New York.

Hoschek S., Carrica P., Weber L. 2008, Bubble Entrainment and Distribution in a Model Spillway with Application to Total Dissolved Gas Minimization, *J. Hydr. Engrg*. 134, 763-771.

Hsiao C., Jain A., Chahine G.L. 2006. Effect of Gas Diffusion on Bubble Entrainment and Dynamics around a Propeller. *26th Symposium on Naval Hydrodynamics*. Rome, Italy.

Hu B., Angeli P., Matar O.K., Lawrence C.J., Hewitt G.F. 2006. Evaluation of Drop Size Distribution from Chord Length Measurements. *AIChE J.* **52**, 931-939.

Hyman, M., 1994. Modeling ship microbubble wakes. CSS/TR-94/39.

Ishii M. 1975. *Thermo-Fluid Dynamic Theory of Two-Phase Flow*, Eyrolles, Paris.

Jeon D., Graff E., Gharib M. 2008. Measurement of Large Scale Bubbly Flows. *27th Symposium on Naval Hydrodynamics*. Seoul, Korea.

Johansen, P.J., Castro, M.A., and Carrica, P.M., 2010. Full-Scale Two-Phase Flow Measurements on Athena Research Vessel. Submitted to: *Int. J. Multiphase Flow*, March 10, 2010.

Latorre, R., Miller, A. and Philips, R., 2003. Micro-bubble resistance reduction on model SES catamaran. *Ocean Eng.* **30**, 2297-2309.

Liu W., Clark N.N. 1995. Relationships Between Distributions of Chords Lengths and Distributions of Bubble Sizes Including their Statistical Parameters. *Int. J. Multiphase Flow* **21**, 1073-1089.

Liu W., Clark N.N., Karamavruc A.I. 1998. Relationship Between Bubble Size Distributions and Chord Length Distribution in Heterogeneously Bubbling Systems. *Chem. Eng. Sci.* **53**, 1267-1276.

Ma J., Oberai A., Drew D., Lahey, R.T. Jr , Hyman M. 2009. A comprehensive subgrid air entrainment model for Reynolds-averaged simulations of free-surface bubbly flows. *62nd Annual Meeting of the APS Division of Fluid Dynamics*. Minneapolis, MN.

McManuels, Terry. "USS Asheville (PG-84)". Patrol Gunboat Reunion Association. 2006 <http://www.gunboatriders.com/theboats/84_asheville/pg84.html>.

Moraga F.J., Carrica P.M., Drew D., Lahey R.T. Jr. 2008. A sub-grid air entrainment model for breaking bow waves and naval surface ships. *Comp. Fluids* **37**, 281-298.

Stutz B., Reboud J.L. 1997. Experiment on unsteady cavitation. *Exp Fluids* 22:191–198.

Takahashi T., Kakugawa A., Makino M., Kodama Y. 2003. Experimental study on scale effect of drag reduction by microbubbles using very large flat plate ships. *J. Kanai Soc. N.A.* **239**, 11-20.

Takeo U.G.A. 1971. Determination of Bubble-Size Distribution in a BWR. *Nucl. Eng. Des.* **22**, 252-261.

Terrill E.J., Fu T. 2008. At-sea measurements for ship hydromechanics. *27th Symposium on Naval Hydrodynamics*. Seoul, Korea.

Terrill E.J., Melville K., Lada G., Otero M., Hazard J., Harris T., Pierson A., Middleton B., Jenkins T. 2005. 2004 Field Measurements. *2005 ONR Bubbly Flows Program Review*. Pasadena, CA.

Vermande S., Simpson K., Essemiani K., Fonade C., Meinhold, J. 2007 Impact of agitation and aeration on hydraulics and oxygen transfer in an aeration ditch: Local and global measurements. *Chem. Eng. Sci.* **62**, 2545-2555.

Xing, Tao. 2009 "Homepage of Tao Xing: Welcome to the world of CFD". Tuskegee University. <http://www.taoxing.net/>.

Yoneda K., Yasuo A., Okawa T. 2002. Flow structure and bubble characteristics of steam-water two-phase flow in a large-diameter pipe. *Nuc. Eng. Des* **217**, 267-281.